Title
Numerical Study of Current Driven Instabilities and Anomalous Electron Transport in Hall-effect Thrusters

Author
Tran, Jonathan

Publication Date
2017

Peer reviewed|Thesis/dissertation

UNIVERSITY OF CALIFORNIA
Los Angeles

Numerical Study of Current Driven Instabilities and Anomalous Electron Transport in Hall-effect Thrusters

A thesis submitted in partial satisfaction
of the requirements for the degree
Master of Science in Aerospace Engineering

by

Jonathan Tran

2017

ABSTRACT OF THE THESIS

Numerical Study of Current Driven Instabilities
and Anomalous Electron Transport in Hall-effect Thrusters

by

Jonathan Tran
Master of Science in Aerospace Engineering
University of California, Los Angeles, 2017
Professor Ann R. Karagozian, Chair

Plasma turbulence and the resulting anomalous electron transport due to azimuthal current driven instabilities in Hall-effect thrusters is a promising candidate for developing predictive models for the observed anomalous transport. A theory for anomalous electron transport and current driven instabilities has been recently studied by [Lafluer et al., 2016a]. Due to the extreme cost of fully resolving the Debye length and plasma frequency, hybrid plasma simulations utilizing kinetic ions and quasi-steady state fluid electrons have long been the principle workhorse methodology for Hall-effect thruster modeling. Using a reduced dimension particle in cell simulation implemented in the Thermophysics Universal Research Framework developed by the Air Force Research Lab, we show collective electron-wave scattering due to large amplitude azimuthal fluctuations of the electric field and the plasma density. These high-frequency and short wavelength fluctuations can lead to an effective cross-field mobility many orders of magnitude larger than what is expected from classical electron-neutral momentum collisions in the low neutral density regime. We further adapt the previous study by [Lampe et al., 1971] and [Stringer, 1964] for related current driven instabilities to electric propulsion relevant mass ratios and conditions. Finally, we conduct a preliminary study of resolving this instability with a modified hybrid simulation with the hope of integration with established hybrid Hall-effect thruster simulations.

The thesis of Jonathan Tran is approved.

Warren B. Mori

Jeff D. Eldredge

Ann R. Karagozian, Committee Chair

University of California, Los Angeles

2017

To my parents . . .

who—among many other things—

saw to it that I learned to touch-type

while I was still in elementary school

Table of Contents

List of Figures

List of Tables

Acknowledgments

I would first like to express my sincere gratitude to my thesis advisor Prof. Ann R. Karagozian of the University of California, Los Angeles Department of Mechanical and Aerospace Engineering for the continued support of my M.S. study and research. Prof. Karagozian's office has always been open whenever I was in need of guidance about my research, coursework or writing and she has been patient and forgiving when dealing with my shortcomings and mistakes. Her knowledge and guidance was essential for the completion of this thesis and I could not have imagined a better advisor and mentor.

Alongside my advisor, I would also like to thank the other members of my thesis committee who offered their time and advice when reviewing this work: Professor Jeff D. Eldredge and Professor Warren Mori of the University of California, Los Angeles, and Dr. Robert R. Martin and Dr. Justin Koo of the Air Force Research Laboratory. Without their passionate participation and input, this thesis could never have been successfully completed.

I would also like to acknowledge Prof. Kentaro Hara of Texas A & M University, Prof. George Morales of the University of California, Los Angeles, the research staff (and interns) at the Air Force Research Lab In-space Propulsion branch, and my fellow lab mates at the Energy and Propulsion Research Laboratory at University of California, Los Angeles for their insightful discussion and comments on the work that has culminated into this thesis. In addition, this work is supported by the Air Force Office of Scientific Research award FA9550-17RQCOR465.

Finally, I must express my very profound gratitude to my parents and to my loving girlfriend for providing me with unfailing support and continuous encouragement throughout my years of study. This accomplishment would not have been possible without them.

Thank you all.

Jonathan Tran

Vita

1990	Born, Riverside, California, USA.
2011–2013	Undergraduate Computational Researcher, Physics Department, California Polytechnic University, Pomona.
2011–2014	Undergraduate Teaching Assistant, Physics Department, California Polytechnic University, Pomona.
2013	B.S. (Physics), California Polytechnic University, Pomona.
2014–present	Computational Plasma Scientist, Air Force Research Lab, In-Space Propulsion Branch, Edwards, California, USA.
2015–present	Graduate Student, Mechanical and Aerospace Engineering Department, University of California, Los Angeles.
2017	M.S. (Mechanical and Aerospace Engineering), University of California, Los Angeles.

Publications

Site Percolation on Lattices with Low Average Coordination Numbers Journal of Statistical Mechanics: Theory and Experiment, 2014(6). doi:10.1088/1742-5468/2014/06/p06014

Percolation Threshold on Three-Dimensional Lattices with Three Nearest Neighbors Journal of Statistical Mechanics: Theory and Experiment, 2013(05). doi:10.1088/1742-5468/2013/05/p05014

CHAPTER 1

Introduction

Spacecraft electric propulsion is a type of propulsion technology which relies on producing thrust by propelling a plasma with an external applied electric and magnetic field. The emergence of Hall-effect thrusters as the leading electric propulsion technology and a history of electric propulsion in general is described in reference [Choueiri, 2004]. As with all forms of electric propulsion, Hall-effect thrusters are characterized as a low thrust device, typically in the range of $40 - 600mN$, with relatively high efficiency and specific impulse (approximately $45 - 60$ percent and $1000 - 10000$ seconds, respectively), thus making it an attractive alternative to chemical thrusters for station-keeping and deep-space scientific applications. The Hall-effect thruster has become a well-established plasma technology for a broad range of spacecraft classes, particularly geosynchronous equatorial orbit communications satellites.

A Hall-effect thruster utilizes a cross-field (perpendicular electric and magnetic fields) discharge described by the Hall effect from which this device has earned its name. A neutral gas propellant is injected at the device anode where it undergoes collisions with electrons trapped within a magnetic field. Xenon propellant is often used due to its high atomic weight, low ionization potential and non-hazardous properties though Hall-effect thrusters have been operated with a variety of propellants, typically heavy gases, most notably Krypton, Argon, Bismuth and Iodine. These collisions ionize the propellant and these ions are accelerated through the truster channel by the electric field. The ions are then neutralized within the plume region with electrons emitted from the cathode. A radial magnetic field with a peak strength of about 100-300 G (0.01-0.03 T) is used to confine the electrons, where the combination of the radial magnetic field and axial electric field cause the electrons to drift in azimuthal direction, thus forming the Hall current. This magnetic field however, is

insufficient for magnetizing the much heavier ions which have a large Larmor-radius (with respect to the length of the Hall-effect thruster channel). Thus, the ions effectively only feel the influence of an electric potential which can have a range of 150-800 volts between the anode and cathode. Because of the azimuthal rotation of the electrons along magnetic field lines, the majority of electrons spend a significant amount of time orbiting a region of high radial magnetic field near the thruster exit plane and a large relative drift velocity between the electrons and ions forms in the azimuthal direction. Collisions with the thruster channel walls and with other species within the plasma, as well as plasma instabilities driven by the azimuthal current can cause the electrons to be freed from the magnetic field and drift towards the anode. This is often referred to as the cross-field electron mobility. Because these electron do not ionize propellent and produce thrust, they are a key factor in limiting the total efficiency of the thruster. The contribution to mobility due to electron particle collisions is well understood and described by [Chen, F. F., 1984] and [Lieberman, M., 1994], however there is an ongoing discussion on the impact of instability driven transport and collisions with the Hall-effect thruster channel walls.

Plasmas with moderate values of the magnetic field such that the ions are weakly magnetized or unmagnetized have distinctly different properties from strongly magnetized plasmas such as those found in fusion applications. Despite the long history of observations, the understanding of Hall plasma turbulence, instabilities and resulting anomalous transport is poor and is lagging behind the progress demonstrated in fusion plasmas. Basic questions of dominant instabilities and dominant range of spatial and temporal scales of fluctuations responsible for the observed level of anomalous electron current and (possibly) heating in Hall devices remains unanswered at a quantitative level. A great deal of research in Hall-effect thrusters is still focused on understanding the anomalous component of the cross-field electron mobility and developing predictive Hall-effect thruster simulations. A considerable effort continues to be made by the community to develop these thruster simulations utilizing a wide range of plasma simulation tools; however, these are typically either (1) multi-fluid or hybrid plasma simulations utilizing kinetic ions and equilibrium fluid electrons which do not accurately capture kinetic effects, (2) reduced dimensional and discount the importance of

azimuthal effects due to geometric symmetry, or (3) do not resolve the time and length scales necessary for a current driven instability. Some notable implementations in the past have been published by [Ahedo and Martinez-Sanchez, 1998], [Boeuf and Garrigues, 1998], and [Barral et al., 2003]. It should be noted that some attempts to simulate Hall-effect thrusters with kinetic methods have been made by [Adam et al., 2004] and [Gildea et al., 2009] however, these attemps continue to struggle with the issues mentioned previously. A commonly used code, HPHall, is a two dimensional (axial and radial), hybrid model developed by [Fife et al., 1997] and has more recently been improved by including sheath effects and channel erosion. Despite this, HPHall and similar simulations continue to struggle with an accurate electron transport model. The shortcomings of these simulations is typically accounted for with an enhanced electron collision rate which is tuned to match experimental measurements, thereby diminishing the predictive capabilities.

We present an initial attempt to further understand the growth and saturation regimes of current driven instabilities and the resultant electron cross-field mobility within a Hall-effect thruster using a simple full kinetic particle in cell simulation. Insights gained from these simulations will direct the focus of the many different numerical implementations in pursuit of a predictive reduced order model of a Hall-effect thruster.

CHAPTER 2

Plasma Theory and Instabilities

Electrostatic plasma instabilities driven by relative electrons and ions drift velocities perpendicular to a magnetic field have been studied by numerous authors across a variety of plasma applications. This cross-field current may be the result of gradients in density, temperature, or in the case of Hall-effect thrusters, the $\mathbf{E} \times \mathbf{B}$ drift. The unmagnetized electron-ion two-stream instability presented by [Buneman, 1963], was one of the first of its kind to be studied and will be investigated in more detail in Section 2.2. The two-stream instability has a large growth rate associated with the wave, on the order of the electron plasma frequency close to the upper hybrid wave, with a weak dependence on mass ratio m_e/m_i. However, the wave is heavily Landau damped if the relative drift velocity v_d is not much larger than the electron thermal velocity v_{T_e}. As a result, the electrons are quickly heated to $v_{T_e} \sim v_d$. In reference [Sagdeev, 1966], it was shown, however, that the system may undergo a mode transition to a low-frequency ion acoustic-like instability driven by density gradients which continue to heat the electrons to $v_{T_e} \geq v_d$. The density gradients can then produce large electric fields, which in turn have numerous consequences on the dynamics of the system. The wave properties and growth rate of the unmagnetized ion acoustic instability are determined from the dispersion relation in Section 2.3. These modified ion acoustic waves can continue to grow until ion temperatures become large enough for ion landau damping to occur. The conditions for this mode transition will be looked at in greater detail in Section 2.5. A recent publication by [Lafleur et al., 2016a] has studied the ion acoustic wave in the context of electron transport within the channel and near-plume of a Hall-effect thruster. This work is of great relevance to the present study. In this chapter we discuss the theory of the linear and nonlinear development of drift instabilities and the impact on the electron dynamics

including quasilinear diffusion, turbulent resonance broadening, and heating, in addition, we will discuss saturation mechanism such as ion trapping and Landau damping.

2.1 Electrostatic Kinetic Equations

The Boltzmann equation is fundamental to kinetic plasma theory and describes the evolution of the plasma distribution function $f(\mathbf{r}, \mathbf{v}, t)$ for particles with velocity $\mathbf{v}$ at coordinates $\mathbf{r}$ and time t; it is given as

$$\frac{\partial f}{\partial t} + \mathbf{v} \cdot \nabla f + \frac{\mathbf{F}}{m} \cdot \frac{\partial f}{\partial \mathbf{v}} = \left(\frac{\partial f}{\partial t}\right)_c \tag{2.1}$$

where $\mathbf{F} = \mathbf{E} + \mathbf{v} \times \mathbf{B}$ is the Lorentz force acting on the particles, $\mathbf{E}$ and $\mathbf{B}$ are the electric and magnetic fields. When describing plasma dynamics such as plasma waves and instabilities on short time-scales ($\tau_{collective} \ll \tau_{collision}$), it is useful to assume $(\partial f/\partial t)_c = 0$. Doing so gives us the Vlasov equation. Perturbation analysis of the Vlasov equation and the electrostatic Maxwell equations ($\mathbf{B} = 0$) gives us a general expression for the Landau dielectric function ϵ in terms of a complex frequency $w = w_R + i\gamma$, where w_R is the real oscillation frequency, γ is the instability growth rate, and $\mathbf{k}$ is the wave number. ϵ then takes the form

$$\epsilon(\mathbf{k}, w) = 1 + \sum_\alpha \frac{q_\alpha^2}{k^2 \epsilon_0 m_\alpha} \int d\mathbf{v} \; \frac{\mathbf{k} \cdot \partial f_\alpha / \partial \mathbf{v}}{w - \mathbf{k} \cdot \mathbf{v}} \tag{2.2}$$

where ϵ_0 is the vacuum permittivity and α is a sum over all the species. The equation for the roots of the dielectric is called the dispersion relation. Defining the real and imaginary parts, $\epsilon_R = \text{Re } \epsilon(\mathbf{k}, w_R + i\gamma)$, $\epsilon_I = \text{Im } \epsilon(\mathbf{k}, w_R + i\gamma)$, and assuming $\epsilon_R > \epsilon_I$ and $w_R > \gamma$, we can use a Taylor-expansion for $\epsilon = \epsilon_R + i\epsilon_I = 0$ for weak instabilities, so that the dispersion relation can be extracted from

$$0 = \epsilon_R(\mathbf{k}, w_R) + i\left(\gamma \frac{\partial}{\partial w_R} \epsilon_R(\mathbf{k}, w_R) + \epsilon_I(\mathbf{k}, \gamma)\right) ... \tag{2.3}$$

Making use of the limit

$$\lim_{\gamma \to 0} \frac{1}{w_R - \mathbf{k} - \mathbf{v}_d + i\gamma} = P \frac{1}{w_R - \mathbf{k} - \mathbf{v}_d} - i\pi\delta(w_R - \mathbf{k} - \mathbf{v}_d) \tag{2.4}$$

where P is the Cauchy principal value, we can set the real and imaginary parts of Eq. (2.3) to zero and have

$$\epsilon_R(\mathbf{k}, w_R) = 1 + \sum_\alpha \frac{w_{p_\alpha}^2}{k^2} P \int d\mathbf{v} \; \frac{\mathbf{k} \cdot \partial f_\alpha / \partial v}{w_R - \mathbf{k}/cdot\mathbf{v}} \tag{2.5}$$

$$\epsilon_I(\mathbf{k}, w_R) = -\gamma \frac{\partial \epsilon_R(\mathbf{k}, w_R)}{\partial w_R} \tag{2.6}$$

Now let us consider the electron and ion species to be a Maxwellian distribution with a thermal velocity $v_{T_\alpha} = \sqrt{\frac{2k_b T_\alpha}{m_\alpha}}$ and a drift velocity of the electron relative to the ions v_d. The distribution function for electrons and ions respectively can thus be written as

$$f_e = \frac{n_e}{\pi^{3/2} v_{T_e}^3} e^{-\frac{(\mathbf{v}-v_d)^2}{v_{T_e}^2}} \qquad \text{and} \qquad f_i = \frac{n_i}{\pi^{3/2} v_{T_i}^3} e^{-\frac{\mathbf{v}^2}{v_{T_i}^2}} \tag{2.7}$$

It is useful to rewrite the velocity integral term of the dielectric function using the plasma dispersion function $Z(\zeta_\alpha)$ and plasma frequency $w_{p_\alpha} = \sqrt{q_\alpha^2 n_\alpha / \epsilon_0 m_\alpha}$. Eq. (2.2) can then be written as

$$\epsilon(\mathbf{k}, w) = 1 + \sum_\alpha \frac{2 w_{p_\alpha}^2}{k^2 v_{T_\alpha}^2} \Big[1 + \zeta_\alpha Z(\zeta_\alpha) \Big] \tag{2.8}$$

where

$$Z(\zeta_\alpha) = \frac{1}{\sqrt{\pi}} \int_{-\infty}^{\infty} \frac{e^{-s^2}}{s - \zeta_\alpha} ds \tag{2.9}$$

$$\zeta_\alpha = \frac{w_R - \mathbf{k} \cdot \mathbf{v}_{d_\alpha} + i\gamma}{k v_{T_\alpha}} \tag{2.10}$$

The plasma dispersion function has no exact analytical solution but for subsequent applications, the asymptotic expansions of $Z(\zeta_\alpha)$ for large and small values of $|\zeta_\alpha|$ become very useful,

$$Z(\zeta_\alpha) = i\sqrt{\pi} e^{-\zeta_\alpha^2} - \begin{cases} \frac{1}{\zeta_\alpha} & \left[1 + \frac{1}{2\zeta_\alpha^2} + \frac{3}{4\zeta_\alpha^4} \dots \right] \qquad \zeta_\alpha \gg 1 \\ 2\zeta_\alpha & \left[1 + \frac{2\zeta_\alpha^2}{3} + \frac{4\zeta_\alpha^4}{15} \dots \right] \qquad \zeta_\alpha \ll 1 \end{cases} \tag{2.11}$$

Note that the $\zeta_\alpha \gg 1$ limit is a valid approximation in the cold-plasma limit, where $v_{T_\alpha} \ll 1$ and minimal Landau damping is expected. As a result we typically neglect the imaginary term in this limit. The equations in this section will be used as building blocks to investigate

the wave and stability properties for drifting Maxwellian distribution is two regimes of practical interest, the drifting ion acoustic wave where $v_d \leq v_{T_e}$ and the electron-ion two-stream instability where $v_d \gg v_{T_e}$.

2.2 Electron-Ion Two-Stream Instability

Following the analysis done by [Krall et al., 1974], Vlasov theory allows a direct calculation of the linear growth of an unstable two-stream distribution. Consider a plasma in Cartesian space where the initial equilibrium distribution for ions and electrons along the $\hat{y}$ direction can be described as two cold Maxwellian distributions drifting relative to one another. The relative drift velocity in the $\hat{y}$ direction between the two species is then v_d and we apply a constraint on the drift velocity $v_d \gg v_{T_e}$.

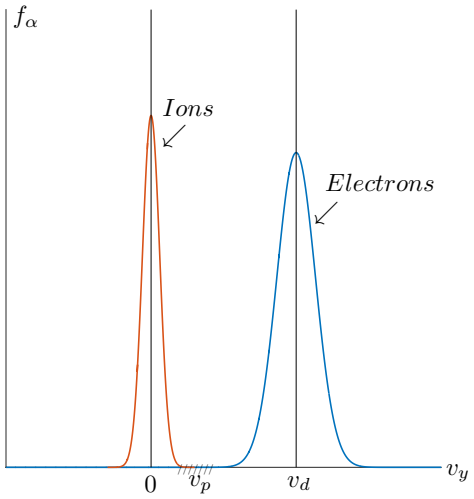

Figure 2.1: Plot of the reduced electron and ion distribution functions $\int\int dv_x dv_z f_\alpha(\mathbf{v})$ in arbitrary units for strong electron-ion two-stream instability. The shaded region denoted by v_p indicates the range where the phase velocity gives positive growth $\gamma > 0$.

Because the two species are assumed cold, we can use the the first two terms of the plasma dispersion function expansion in Eq. (2.11) for $|\zeta_e| \gg 1$ and $|\zeta_i| \gg 1$ to show

$$\tilde{\epsilon}(\mathbf{k}, w) = 1 - \frac{w_{pe}^2}{(w_R - kv_d + i\gamma)^2} - \frac{w_{pi}^2}{(w_R + i\gamma)^2} \tag{2.12}$$

knowing $\mathbf{k} \cdot \mathbf{v}_d \approx kv_d$. This dielectric equation has four solutions when $\tilde{\epsilon}(\mathbf{k}, w) = 0$ for the

complex oscillation frequency w. Two branches correspond to stable oscillations where $\gamma = 0$ and the other two solutions form conjugate pairs. It can be shown that the unstable branch exhibits growth ($\gamma > 0$) for wavenumber k in the range

$$0 < |kv_d| < w_{p_e}\left[1 + (w_{p_i}^2/w_{p_e}^2)^{1/3}\right]^{3/2} \tag{2.13}$$

Solving Eq. 2.6 for γ and applying $\partial\gamma/dk = 0$, the wavelength corresponding to the maximum growth rate can be approximately determined as

$$k_{max} \approx w_{pe}/v_d \tag{2.14}$$

and the dispersion relation can then be solved for the maximum wave frequency and growth rate as

$$[w_R]_{max} \approx \frac{1}{2}\left(\frac{w_{p_i}^2}{2w_{p_e}^2}\right)^{1/3} w_{p_e} \tag{2.15}$$

$$\gamma_{max} \approx \sqrt{3}\left(\frac{w_{p_i}^2}{2w_{p_e}^2}\right)^{1/3} w_{p_e}^{1/2} \tag{2.16}$$

which has a linear growth rate with a weak dependence on the mass ratio of the plasma species. The phase velocity of the wave is nearly the relative drift velocity of electrons $v_p = w_R/k \approx v_d$. The Buneman instability, as it is sometimes referred to as, is a high frequency mode which acts to heats the electrons to $v_{T_e} \sim v_d$ on a time scale on the order of $\tau_b = 2\pi/w_I$, which is significantly faster than any relevant ion time scale. The wave energy ($U_E = \sum_k \mathbf{E}_k^2/8\pi$) also increases at a rate comparable to the electron heating. [Davidson, 1972] confirms these results and shows via numerical simulations a stage of growth where electrons are trapped in an electrostatic wave. At saturation, after multiple τ_b, the electron-ion distribution appears multi-peaked but in actuality is stable i.e. ($f(v) = f_e + (m_e/m_i)f_i$ is monotone-decreasing) and the electrostatic energy has stopped increasing over time.

Finally, the dielectric equation in Eq. 2.12 neglects any Landau damping effects by the plasma ions. The wave properties corresponding to the maximum growth rate are valid approximations provided the ions are sufficiently cold such that

$$\frac{v_d}{v_{T_i}} \gg \left(\frac{m_e}{2m_i}\right)^{1/3} \tag{2.17}$$

2.3 Ion Acoustic Instability

In this section, we consider the electrostatic stability properties for electrons drifting through background plasma ion where the relative streaming velocity is small or on the order of the thermal velocity. Similar to the analysis done before, the equilibrium distribution functions can be represented as a Maxwellian, however in the present analysis, $T_e \gg T_i$. Previous studies of the ion acoustic wave by [Fried and Conte, 1961] has shown that, in the absence of drift, the ion acoustic wave is damped and stable. We now wish to investigate whether the presence of an electron-ion drift (which is associated with a net current flowing in the plasma) can destabilize the mode.

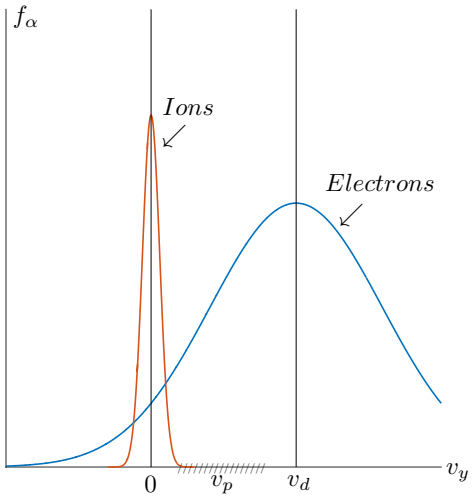

Figure 2.2: Plot of the reduced electron and ion distribution functions $\int\int dv_x dv_z f_\alpha(\mathbf{v})$ in arbitrary units for the ion acoustic instability. The shaded region denoted by v_p indicates the range where the phase velocity gives positive growth $\gamma > 0$.

The assumptions made on the ion's plasma dispersion function remain the same, i.e. $\zeta_i \gg 1$, however for the ion acoustic wave, $\zeta_e \ll 1$. The dielectric function in Eq. (2.8) in terms of the expanded plasma dispersion functions for $|\gamma/w_R| \ll 1$ is then

$$\epsilon(\mathbf{k}, w_R + i\gamma) = 1 + \frac{1}{k^2\lambda^2} - \frac{w_{pi}^2}{(w_R + i\gamma)^2} + i\frac{2\pi w_{pe}^2}{kv_{T_e}}\left(\frac{w_R - kv_d + i\gamma}{kv_{T_e}}\right)e^{-\left(\frac{w_R - kv_d + i\gamma}{kv_{T_e}}\right)} \tag{2.18}$$

and

$$\epsilon_R(\mathbf{k}, w_R + i\gamma) = 1 + \frac{1}{k^2\lambda^2} - \frac{w_{pi}^2}{w_R^2} \tag{2.19}$$

where $\lambda = v_{T_e}/w_{p_e} = \sqrt{\epsilon_0 T_e/q_e n_e}$ is the electron Debye length and the phase velocity lies within the range $|w_R/k| \gg v_{T_i}$ and $|w_R/k - v_d| \ll v_{T_e}$. Solving $\epsilon_R(k, w_R) = 0$ for the wave frequency, we obtain

$$w_R^2 = \frac{k^2 c_s^2}{1 + k^2\lambda^2} \tag{2.20}$$

where $c_s = w_{p_i}\lambda_d = \sqrt{k_b T_e/m_i}$ is the ion sound speed. To evaluate the growth rate γ, we make use of Eq. 2.6 and 2.19.

$$\frac{\partial \epsilon_R}{\partial w_R} = -\frac{2w_{p_i}^2}{w_R^3} \tag{2.21}$$

$$\epsilon_I(k, w_R) = -\pi \sum_\alpha \frac{w_{p_\alpha}^2}{k^2} \int d^3v \; \delta(w_R - kv_d) k \frac{\partial}{\partial v} f_\alpha(v) \tag{2.22}$$

$$\gamma = \left(\frac{\pi}{8}\right)^{1/2} \frac{|w_R|}{(1 + k^2\lambda_d^2)^{3/2}} \left[\left(\frac{m_e}{m_i}\right)^{1/2} \left(\frac{kv_d}{w_R} - 1\right) - \left(\frac{T_e}{T_i}\right)^{3/2} e^{-\frac{T_e}{2T_i(1+k^2\lambda_d^2)}} \right] \tag{2.23}$$

It should be said that the contribution of the ion temperature to the growth rate always corresponds to damping of the instability, that is, when $T_e/T_i \gg 1$, ion Landau damping is exponentially small. As T_e/T_i approaches order unity the assumption $\zeta_i \gg 1$ is no longer valid and the ion acoustic wave is heavily damped. The value of T_e/T_i at which the instability ceases to grow is more nuanced and will be discussed in the following section. The electron contribution to the growth rate corresponds to growth or damping depending on the sign of $kv_d/w_R - 1$.

If we assume $T_e/T_i \gg 1$ and $v_d = 0$, we have the well known solution for weakly damped ion waves. This damping is due to interactions of ions moving with velocities close to the phase velocity, with a rate shown by many authors to be

$$\gamma = -\left(\frac{\pi m_e}{8m_i}\right)^{1/2} \frac{|k| c_s}{(1 + k^2\lambda^2)^2} \tag{2.24}$$

Allowing a drift velocity larger than the phase velocity, i.e. $|v_d| > w_R/k$, predicts growth of the instability ($\gamma > 0$). The growth rate can be approximated as

$$\gamma = \left(\frac{\pi m_e}{8m_i}\right)^{1/2} \frac{|w_R|}{(1 + k^2\lambda^2)^{3/2}} \left(\frac{kv_d}{w_R} - 1\right) \tag{2.25}$$

Using an analysis similar to Section 2.2, from $\partial\gamma/\partial k = 0$ we can approximate the wave number, wave frequency, and growth rate corresponding to the maximum growth rate from

Eq. (2.25) as

$$k_{max} \approx \frac{1}{\sqrt{2}\lambda}, \quad [w_R]_{max} \approx \frac{w_{p_i}}{\sqrt{3}}, \quad \text{and } \gamma_{max} \approx \sqrt{\frac{\pi m_e}{54 m_i}} \frac{v_d}{\lambda} \tag{2.26}$$

where the phase velocity can be estimated to be $v_p = \sqrt{\frac{2}{3}} c_s$.

The ion acoustic wave is thus a low frequency longitudinal oscillation similar to an acoustic wave traveling in a neutral gas. However, since the waves propagate through positively charged ion density perturbations, the waves interact with electromagnetic fields, thereby coupling to the electrons. This coupling allows the wave to exist in the absence of collisions. The electric field produced by the density fluctuations of the ion acoustic wave also have a significant impact on the dynamics of the electrons.

2.4 Beam Cyclotron Instability

If we now consider a moderate magnetic field **B** capable of magnetizing the electron while the ions remain unmagnetized, the electron drift relative to ions across magnetic field lines is $v_d = |\mathbf{E}|/|\mathbf{B}|$. The electron-ion two stream instability and the ion acoustic wave discussed in the previous two sections continue to persist in addition to new collective instabilities due to resonant coupling of the ion mode and an electron cyclotron mode due to the magnetic field. The dispersion relation for a plasma in a magnetic field has been previously derived by [Lampe et al., 1971] and [Tsikata et al., 2014], who commonly refer to the instability as a beam cyclotron instability. In these works, the authors show the effect of the magnetic field is to quantize the dispersion relation with discrete wave frequencies and growth rates in **k** space. These bands are centered on the cyclotron harmonics, $w_R = n\Omega_e$, $k = n\Omega_e/[v_d - c_s(1+k^2\lambda^2)^{1/2}]$ with bandwidths given by $\delta w \simeq 2\gamma$ and $\delta k \simeq 2\delta w/v_d$ for integer n. However, this discrete nature only becomes significant when the wave number parallel to the magnetic field is very small. The work presented here assumes this parallel wave number is, in fact, negligible and the high frequency behavior and wave properties can then be approximated using the electron-ion two-stream instability equations. For larger wave numbers, the time scales of interest are significantly larger than the cyclotron frequency. As a result, the dispersion relation simplifies to the ion acoustic type relation also discussed in Section (2.3). The appendix of [Lafleur et al., 2016a] confirms that this assumption is valid.

2.5 Mode Transition and Condition for Instability

We can see there is a very close relationship between the electron-ion two stream instability and the ion acoustic wave. From the previous sections we show that when both plasma species are cold and the electrons stream relative to ions (similar to Fig 2.1) due to a moderate magnetic field, two distinct stages of quasilinear development are possible: the beam cyclotron instability for low levels of turbulence, and the ion acoustic instability.

When the drift velocity is larger than the electron thermal velocity, we first encounter a beam cyclotron instability with a growth rate proportional to $\gamma \propto (m_i/m_e)^{1/3} w_{p_e}^{1/2}$. From [Dum, 1970] the beam cyclotron instability creates turbulent electric fields perpendicular to **B** and parallel to the drifting electrons. Due to these turbulent azimuthal electric fields, the electrons no longer have a well-defined gyro-orbit. Instead, there is additional cross field spatial diffusion where the diffusion coefficient D is proportional to the electrostatic field energy $\langle E^2 \rangle$. As a result, the electron gyroresonances are broadened by a frequency $\Delta w = k^2 D$ and the electrons are heated to $v_{T_e} \sim v_d$. When the turbulent fields become so large that electrons diffuse a distance of the order of a wavelength in a gyrotime $1/\Omega_e$, nonlinear analysis by [Lampe et al., 1971] show that the electron cyclotron instability becomes an ordinary ion sound instability. This transition happens approximately when the electric potential satisfies the equation

$$e\phi/T_e \approx 2(2/\pi)^{3/4}(\Omega_e/w_e)\left[\left(\frac{kv_d}{\Omega_e}\right)^{1/2}(k\lambda)\right]^{-1} \tag{2.27}$$

and occurs on a time scale typically much faster than any relevant ion time scale as we will see in our simulation.

The ion acoustic instability is a resonant particle instability which is driven by the electrons and has a growth rate γ proportional to $(m_i/m_e)^{1/2}(v_d/c_s)w_{p_i}^{1/2}$. This transition is extremely important, as we will show later, because the ion acoustic wave can continue to heat electron well beyond $v_{T_e} \sim v_d$ and cause bunching of the ions leading to large fluctuations in electric fields perpendicular to **B**. However, as we have shown before, the ion acoustic wave becomes ion Landau damped when T_i/T_e is large and the beam cyclotron modes will stabilize at or before the time scale in Eq. (2.27). If T_i/T_e is small, Eq. (2.27) represents a

mode transition to an ion acoustic wave where a second period of exponential wave growth ensues at the ion sound growth rate which is smaller than the beam cyclotron growth rate. The criterion for this transition is much more nuanced and described in much more detail by [Stringer, 1964]. For the work done here, an approximate criterion for stability is

$$\frac{T_i}{T_e} \geq \frac{v_d}{v_{T_e}} \tag{2.28}$$

When the fluctuations in electric field become large enough to trap ions, the ion acoustic instability saturates and the ion distribution fluctuates between growth and Landau damping. According to [Lafleur et al., 2016b] this occurs roughly at

$$\delta\phi \approx \frac{1}{2}\frac{m_i}{q_i}v_p^2 \tag{2.29}$$

To summarize the kinetic analysis of drifting plasmas, in both stages, energy is extracted from the drifting motion, which causes the electron temperature, ion temperature, and electrostatic energy to all grow exponentially at different rates. The difference here is that the growth rates of the electron-ion instability are considerably larger than those for the ion acoustic as we have previously shown. [Lampe et al., 1971] describe three different methods by which a drifting plasma may achieve stability: (1) Linearly, where the drift velocity is insufficient to produce exponential growth in the electron-ion instability, the wave growth and electron heating will cease; (2) Resonance Broadening, where T_i/T_e is too large given by Eq (2.28), and a transition to a stable ion acoustic wave ends the instability; and (3) Ion Trapping, where the ion acoustic instability grows, a tail is developed in the ion velocity distribution function due to ion trapping and is no longer Maxwellian. The distribution tail then resonates with the phase velocity and the plasma is Landau damped.

2.6 Electron Mobility

An understanding of the impact of drift instabilities allows us to discuss the effects on electron mobility in the context of a Hall-effect thruster. To obtain the equations for mobility, we return to the Boltzmann equation in Section 2.1. The observable parameters in our plasma can be obtained by taking moments of our plasma distribution function $f(\mathbf{r}, \mathbf{v}, t)$:

$$n(\mathbf{r}, t) = \int f(\mathbf{r}, \mathbf{v}, t) d\mathbf{v}$$

$$\bar{v}(\mathbf{r}, t) = \int \mathbf{v} f(\mathbf{r}, \mathbf{v}, t) d\mathbf{v}$$

$$\bar{v}^2(\mathbf{r}, t) = \int \mathbf{v}^2 f(\mathbf{r}, \mathbf{v}, t) d\mathbf{v}$$

Similarly, the moments of our Boltzmann equation are used to derive the plasma fluid equations. These equations are useful for modeling plasmas near equilibrium where the distribution function can be approximated as Maxwellian. The continuity and momentum equations are given as

$$\frac{\partial n}{\partial t} + \nabla \cdot (n\bar{v}) = 0 \tag{2.30}$$

$$\frac{\partial}{\partial t}(mn\mathbf{v}) + \nabla \cdot (mn\mathbf{v}\mathbf{v}) = qn\mathbf{F} - \nabla \cdot \Pi + \mathbf{P}_{ij} \tag{2.31}$$

Consider the momentum conservation equation for electrons where the stress tensor $\mathbf{P}_{ij}$ reduces to the momentum exchange interaction between electrons and neutrals with a collision frequency of ν_{en}

$$\frac{\partial}{\partial t}(m_e n_e \mathbf{v_e}) + \nabla \cdot (m_e n_e \mathbf{v_e} \mathbf{v_e}) = q_e n_e (\mathbf{E} + \mathbf{v} \times \mathbf{B}) - \nabla \cdot \Pi - m_e \nu_{en} n_e \mathbf{v_e} \tag{2.32}$$

We can neglect the inertial and pressure terms and from the Hall-effect thruster geometry in Fig 2.3, we reduce the magnetic field to zeroth order by ignoring fluctuations due to current densities. The magnetic field becomes $\mathbf{B} \rightarrow B_x$ and the momentum equation in component form becomes

$$0 = q_e n_e E_x - m_e \nu_{en} n_e v_x$$

$$0 = q_e n_e E_y - q_e n_e v_z B_x - m_e \nu_{en} n_e v_y$$

$$0 = q_e n_e E_z - q_e n_e v_y B_x - m_e \nu_{en} n_e v_z$$

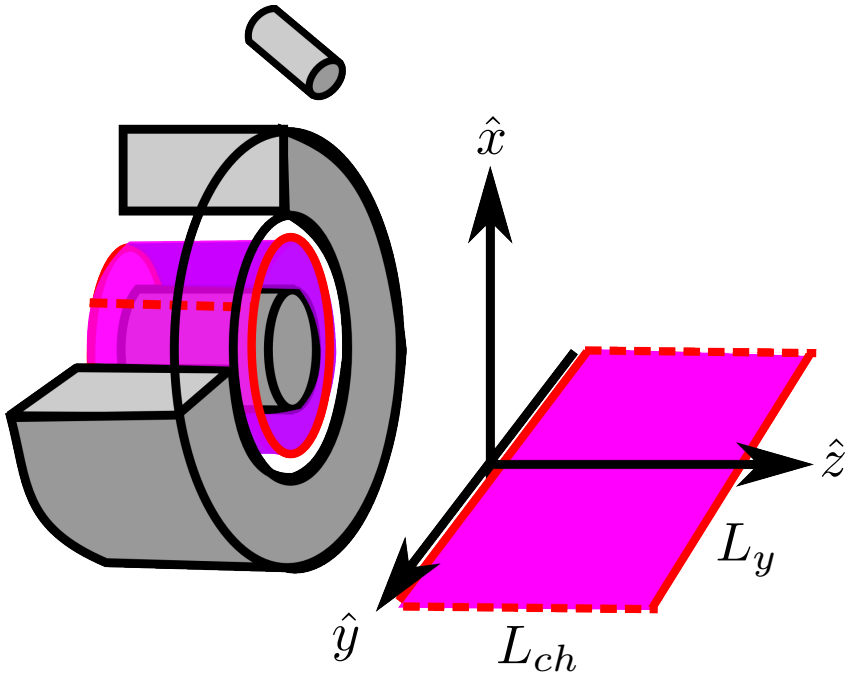

Figure 2.3: Schematic of a Hall-effect thruster showing the relevant field and simulation directions and the simplified $y-z$ simulation plane. A uniform magnetic field B_0 is in the $\hat{x}$ direction and a uniform electric field E_0 in the $\hat{z}$ direction. The electron drift velocity and direction of the fluctuating electric field is then in the $\hat{y}$ direction.

We can perform a similar treatment to the electric field as the magnetic field and reduce it to only the applied electric field in the axial direction $\mathbf{E} \rightarrow E_z$. Doing so, we can solve for the classical cross field mobility in terms of the axial electron flux $\Gamma_z = n_e v_z$

$$\mu_\perp = \frac{\Gamma_z}{E_z} = \frac{\frac{|q_e|}{m\nu_{en}}}{1 + \frac{w_{ce}^2}{\nu_{en}^2}} \tag{2.33}$$

If we do not neglect the fluctuations in electric field and electron density in the azimuthal direction and instead consider an average of these two quantities $< n_e E_y >$, the y-component of the momentum equation becomes

$$0 = q_e \langle n_e E_y \rangle - q_e n_e v_z B_x - m_e \nu_{en} n_e v_y$$

and we can solve for an effective cross field mobility

$$\mu_{\langle n_e E_y \rangle} = \mu_\perp \left[1 - \frac{w_{ce}}{\nu_{en}} \frac{\langle n_e E_y \rangle}{n_e E_z} \right] \tag{2.34}$$

In the limit $\nu_{en} \to 0$, we have $\mu_\perp \to 0$ from Eq. (2.33). With the modified mobility in Eq. (2.34), we now have $\mu_{eff} \to -\frac{<n_e E_y>}{n_e E_z B_x}$ which puts a floor on the mobility for low neutral pressures where the collision frequency in negligible (the correlation term $\langle n_e E_y \rangle$ is negative and associated with electron wave scattering). The spatiotemporal averaging of fluctuating quantities can be interpreted as

$$\langle g(\mathbf{r},t) \rangle = \int_0^L \frac{d\mathbf{r}}{L} \int_0^T \frac{dt}{T} g(\mathbf{r},t) \tag{2.35}$$

Ongoing discussion with Prof. Kentaro Hara has led to another method of approximating the electron mobility due to these azimuthal waves. Considering the differential form of Gauss' Law, $\nabla \cdot \mathbf{E} = \frac{|q_e|}{\epsilon_0}(n_i - n_e)$, we can rewrite the averaged electron density and azimuthal electric field as

$$\langle n_e E_y \rangle = \langle n_i E_y \rangle - \frac{\epsilon_0}{2|q_e|} \langle \frac{\partial}{\partial y} E_y^2 \rangle \tag{2.36}$$

If we then interpret the second term on the right hand side and apply the spacial averaging integral over a periodic space, we find this quantity is conserved. As a result

$$\langle n_e E_y \rangle = \langle n_i E_y \rangle \tag{2.37}$$

$$\mu_{\langle n_i E_y \rangle} = \mu_\perp \Big[1 - \frac{w_{ce}}{\nu_{en}} \frac{\langle n_i E_y \rangle}{n_e E_z} \Big] \tag{2.38}$$

It is important to note that the effective mobility calculated with either $\langle n_e E_y \rangle$ or $\langle n_i E_y \rangle$ is only true when the averaging is done over a wave period and wavelength which is periodic. When averaging over small regions in space, one will need to consider the gradient of the wave energy density. Lastly, an additional method of empirically obtaining effective mobility from simulation data can be acquired by averaging the axial velocity v_z and using the expression

$$\mu_{(v_z/E_z)} = \frac{\langle v_z \rangle}{E_0} \tag{2.39}$$

CHAPTER 3

Description of Simulations

3.1 Thermophysics Universal Research Framework

As mentioned in previous chapters, this study is done in collaboration with the In-Space Propulsion Branch (RQRS) at Edwards Air Force Research Laboratory (AFRL). The primary research focus of RQRS is electric propulsion devices and a great deal of effort is put into Hall-effect thruster and plasma plume simulations. These plasma plume simulations are particularly useful for investigating plume/spacecraft interaction including sputtering, charging, and redeposition of material on the spacecraft components and have been an integral part of the modeling and simulation group. Through collaboration among AFRL and a number of authors including [Fife and Martinez-Sanchez, 1998] and [Brieda, 2005], DRACO was developed in 2003 as a major component of the legacy COLISEUM plasma simulation package, with the goal of simulating plume-spacecraft interactions. Until recently, DRACO has been the primary tool used to investigate plume simulations. RQRS is currently in development of the Thermophysics Universal Research Framework (TURF) which will be capable of simulating plasmas in a wide range of conditions, length scales and time scales utilizing both kinetic and fluid methods. While still being in the early stages of development, the first implementation of TURF facilitated a direct replacement for the plume simulation code DRACO and supporting it's critical functionality. Reference [Araki et al., 2016] has obtained good agreement between the two codes. With the framework set in place, the developers of TURF are currently in the process of expanding its capabilities.

In an effort to study the numerous velocity space instabilities which may arise within the channel region of the Hall-effect thruster, TURF functionality was augmented to facilitate

modeling of magnetized kinetic electrons. We make use of the kinetic plasma simulation technique, particle in cell (PIC) simulations described in [Birdsall and Langdon, 1991]. In this method, individual particles are tracked discretely through phase space (Lagrangian), whereas moments of the distribution such as densities and currents are computed simultaneously on spatially defined mesh points (Eulerian). Kinetic models such as these are generally more computationally intensive than fluid models since hundreds of particles are needed per cell to suppress numerical noise. Fully kinetic simulations of Hall-effect thrusters where both the ions and electrons are modeled with PIC techniques are also particularly difficult to implement due to the large difference in time scales between the electron and ion behavior at Hall-effect thruster relevant densities, time, and length scales. Despite this, kinetic methods are the standard for studying velocity-space instabilities in collisionless plasmas which we plan to investigate. While the current focus of TURF is hybrid simulations (fluid electron/kinetic ion) of spacecraft plume interactions, a number of validation and verification cases have been benchmarked for full kinetic plasma simulations when $\mathbf{B} = 0$ including the collisionless electrostatic shock and glow discharge. All simulations in this body of work are completed within the TURF framework. In the following sections we demonstrate extended functionality through the implementations and modules recently developed within TURF and its capability to perform kinetic simulations of magnetized electrostatic plasmas.

3.2 Anomalous Electron Transport Simulation

In order to study the effects of current driven instabilities on the cross field electron transport within a Hall-effect thruster, we have implemented a simplified PIC simulation presented by [Lafleur et al., 2016b] and [Boeuf, 2014]. The coordinate system is identical to Fig. (2.3), where the cylindrical geometry of a HET is unraveled into periodic cartesian space. A uniform magnetic field is imposed in the $\hat{x}$ direction and a uniform electric field in the $\hat{z}$ direction. As a result, the azimuthal or $\hat{y}$ direction corresponds to the $\mathbf{E} \times \mathbf{B}$ drift direction. An azimuthal electric field component is then obtained by solving Poisson's equation in 1D. For this cartesian approximation to be valid, the simulated azimuthal length L_y must be

small when compared to the physical length around the channel. TURF is inherently a three dimensional framework, and as a result, positions and velocities of both particle species are then tracked in all three directions and are updated using the standard Boris push algorithm outlined in [Birdsall and Langdon, 1991] which has been incorporated into TURF for these simulations. The particles are then weighted onto a grid in the $\hat{y}$ direction (regardless of the position in the $\hat{x}$ or $\hat{z}$) to determine charge densities for solving Poisson's equation using a finite difference, direct tri-diagonal solve. The plasma is assumed to be fully ionized in that only electrons and singly charged xenon ions are modeled. Both electrons and ions are advanced with Boris and the plasma is assumed to be collisionless (though TURF has the capability to model electron-neutral elastic scattering, change exchange, Coulomb collisions and ionization collisions).

3.2.1 Boundary Conditions

Periodic boundary conditions are used for both the particles and fields in the two directions perpendicular to the electric field $\hat{x}$ and $\hat{y}$ and a *stream* boundary condition is used in the direction of the electric field $\hat{z}$. The *stream* boundary condition on the particles acts to maintain constant plasma density within the simulation. When a electron or ion exits the simulation in either the positive or negative $\hat{z}$ direction, it is reintroduced on the low or high potential boundary respectively with a randomized position in $\hat{x}$ and $\hat{y}$ position. The velocity is then sampled from a Maxwellian velocity distribution at a constant temperature and drift velocity. The injection drift velocity is typically set to zero and the injection temperature is set to the temperature of the initial condition for each species respectively. In reference [Lafleur et al., 2016b], it was shown this boundary condition is sufficient for limiting the growth on electron and ion energy in axial direction when a driving force E_0 is applied. Because the electrons undergo cyclotron motion, they are injected a small distance away from the domain boundary to prevent immediate interaction with the same boundary. Though a minor discrepancy, we are unsure if [Lafleur et al., 2016b] had accounted for this behavior. It was incorporated in the model since we observed numerous simulations showing filtering of hot electrons by the boundary condition. As a result, the actual injection temperature was

significantly smaller than intended and electrons would remain trapped near the boundary. We expect the offset of the injection region for electrons should have no impact on the field calculation of simulation due to the Poisson equation not being solved in the axial direction.

3.2.2 Initial Conditions

Modifications to the approach in [Lafleur et al., 2016b] have also been made to the initial conditions. The initial electrons are distributed uniformly throughout the simulation domain with a constant temperature. When the ions are distributed uniformly in space like the electrons, we observe a surging of ions in the axial direction as they develop towards a parabolic spacial profile but interact with the axial boundary condition. Though this is not significant for the field calculation, we detect large non-physical fluctuations in ion temperature corresponding to the convection time of the ions. Since we wish to investigate the evolution of ion thermal energy, the initial ions are distributed with a parabolic density and velocity distribution (in addition to a Maxwellian thermal velocity) in the axial direction under the force of the applied electric field. This is done by sampling a random time between $0 < t_r < \tau_g$ where τ_g is the time for the ions to be convected away (leave the simulation). The position and velocity for each particle in the $\hat{z}$ is then determined with the simple equation

$$z = \frac{q_i}{2m} E_0 t_r^2 \quad \text{and} \quad v_z = E_0 t_r + v_s \tag{3.1}$$

where v_s is the velocity sampled from the thermal distribution. The position in the $\hat{x}$ and $\hat{y}$ directions remain uniform and the velocities remain Maxwellian. It is important to note this initial condition only considers ions in an unmagnetized configuration. This is only a minor issue because the Larmour radius is large compared to the axial channel length, i.e. $r_L \gg L_{ch}$.

We have found this is a sufficient way to reduce the surging of ions though the axial boundary condition. Phase space in the $\hat{y}$ and $\hat{z}$ directions of the initial electron and ion distributions are plotted in Figure 3.1 and 3.2 for clarity. Phase space in the radial direction $\hat{x}$ is identical to Figure 3.2 when normalized in space by L_x.

3.3 Operating Conditions

The normal operating conditions for our simulations are consistent with [Lafleur et al., 2016b] and are presented in Table 3.1. From the given plasma parameters, the drift velocity $v_d = E_0/B_0 = 1.0e6\ m/s$ is much larger then either the electron or ion thermal velocity. As a result, the tabulated plasma conditions are sufficient for instigating the initial beam cyclotron instability. The moderate strength of the magnetic field also produces an ion gyroradius $r_g = m_i v_\perp / q_i B$ which is significantly large when compared to the length of the channel.

The numerical operating conditions used ensure resolution of both the Debye length (in the azimuthal direction) and the electron plasma frequency. The grid size is set such that the CFL condition is met even at saturation when electron temperatures are much higher. In the $\hat{x}$ and $\hat{z}$ directions the domain acts as a single cell. The length of the domain must satisfy the constraint of being larger than the quantized wave numbers discussed in Section (2.4). Unless otherwise stated, parameters outlined in this section and shown in Table 3.1 will serve as the baseline operating conditions for our results.

Plasma Parameter	Description	Value
n_0 ($\# \ m^{-3}$)	Plasma Density	1.0e17
B_0 (T)	Applied Magnetic Field	2.0e-2
E_0 (Vm^{-1})	Applied Electric Field	2.0e4
T_{e_0} (eV)	Initial Electron Temperature	2.0
T_{i_0} (eV)	Initial Ion Temperature	0.1
Numerical Parameter	**Description**	**Value**
δt (s)	Timestep	5.0e-12
L_x (m)	Radial Length	2.5e-5
L_y (m)	Azimuthal Length	0.5e-2
L_{ch} (m)	Channel (Axial) Length	1.0e-2
NG	Grid Points	200
N/NG	Computational Particles per Cell	500

Table 3.1: The standard plasma parameters and numerical constraints are consistent with [Lafleur et al., 2016b] and [Boeuf, 2014].

3.4 Electron Resampling

Historically, due to the computational cost of full kinetic simulations, the Hall-effect thruster community has typically utilized either hybrid or multi-fluid methods when modeling the channel of the thruster. [Fife and Martinez-Sanchez, 1998], [Koo and Boyd, 2006], and [Mikellides and Kat have presented some of the many different implementations of Hall-effect thruster simulations. While still utilizing the full kinetic simulation description we have implemented, we hope to investigate whether the azimuthal instabilities can be resolved when retaining only the first moments of the electron velocity distribution function. By resampling the electron velocity distribution function every iteration after the Boris push (using the electron temperature and drift velocity calculated within the cell) we hope to remove any kinetic information and treat the electrons as *fluid-like*. The electron positions are not updated in this process, keeping any density fluctuations which may arise due to the instabilities. We would like to

note that, as one would expect, this procedure makes the simulations more computationally intensive and is meant only as a proof of concept.

Early implementations of this model revealed that numerical heating and error accumulation in the mean velocity posed a significant issue. As illustrated in Figure 3.3, resampling with small populations of electrons can cause a random walk of the mean velocity and standard deviation, especially over a large number of resampling n_s, as shown in Figure 3.4. In order to conserve momentum and energy during the resampling, we rescale the velocity of each particle after resampling using the equation

$$v_e^* = \sqrt{\frac{T_e^*}{T_e}}(v_e - \bar{v}_e) + \bar{v}_e^* \tag{3.2}$$

where $*$ indicates the expected value.

The addition of this procedure, which we will call the moment method, to our baseline simulation will hopefully give insight to the possibility of resolving the beam cyclotron and ion acoustic instability with a hybrid fluid electron kinetic ion method.

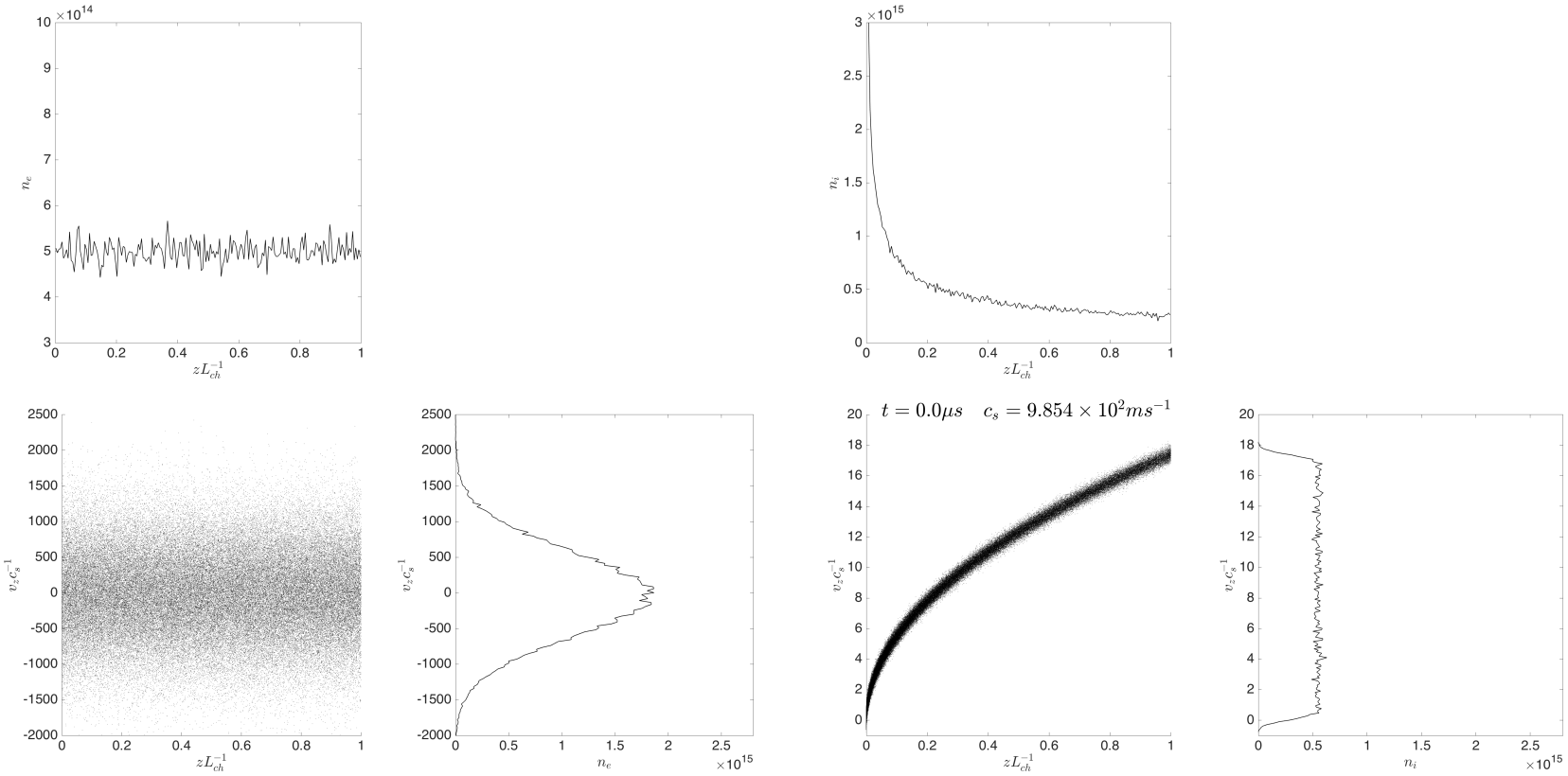

Figure 3.1: Phase space and corresponding distribution function of the initial $t = 0$ state for the baseline operating conditions. For the given electron temperature and Xenon mass, the velocity is normalized by the ion sound speed $c_s = 9.854 \times 10^2$ and the position is normalized by L_{ch}. The figures are presented in sets of three: a phase space diagram, a velocity distribution function, and a position distribution function. On the left, we have the electron phase space in the $\hat{z}$ direction. The electron velocity distribution is Maxwellian and spacial distribution function is uniform in the $\hat{z}$ direction. On the right ion phase space in the $\hat{z}$ direction. The ion velocity distribution is uniform while the position distribution function is parabolic in the $\hat{z}$ direction.

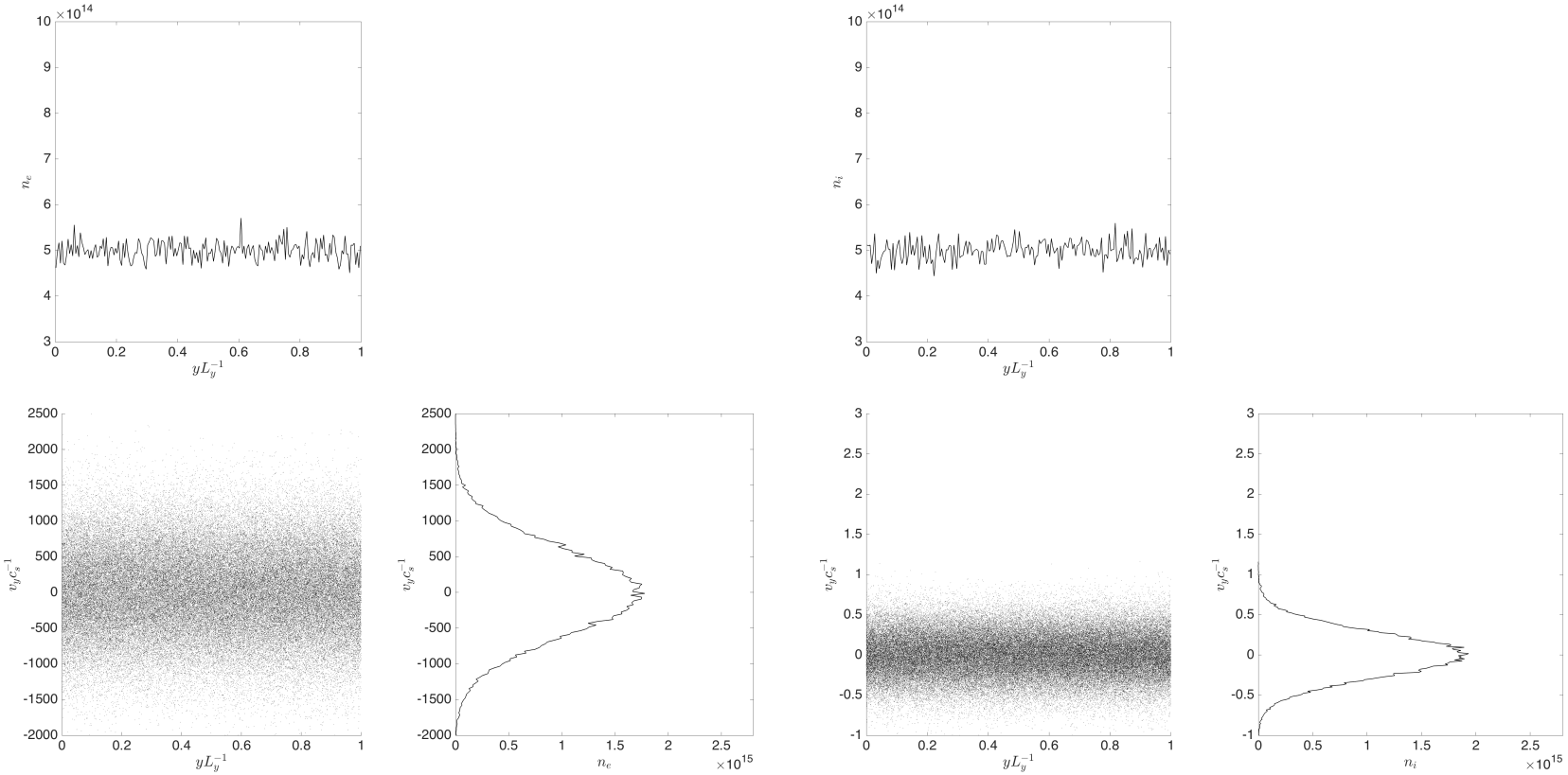

Figure 3.2: Phase space and corresponding distribution function of the initial $t = 0$ state for the baseline operating conditions. For the given electron temperature and Xenon mass, the velocity is normalized by the ion sound speed $c_s = 9.854 \times 10^2$ and the position is normalized by L_y. The figures are presented in sets of three: a phase space diagram, a velocity distribution function, and a position distribution function. On the left we have the electron phase space in the $\hat{y}$ direction. The electron velocity distribution is Maxwellian and the spacial distribution function is uniform in the $\hat{y}$ direction. On the right we have the ion phase space in the $\hat{y}$ direction. The ion velocity distribution is Maxwellian and the position distribution function is uniform in the $\hat{y}$ direction.

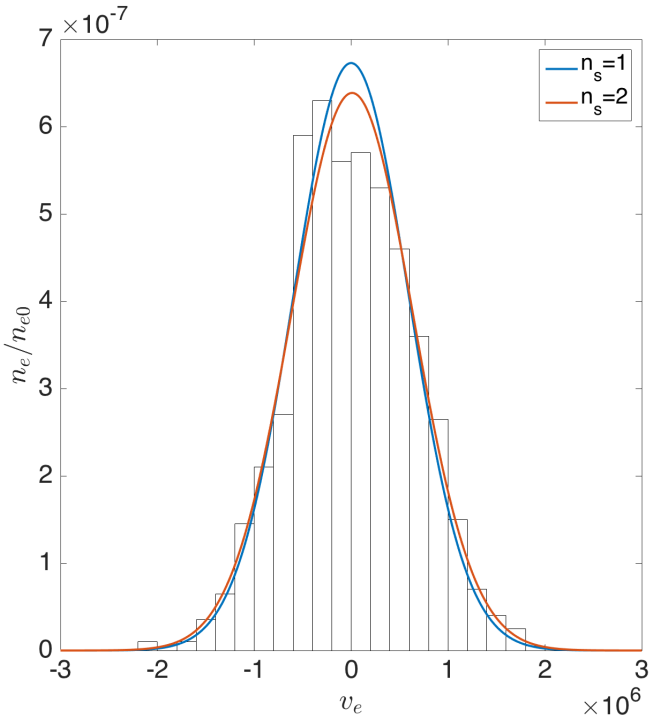

Figure 3.3: Illustration of numerical error in temperature and drift velocity accrued by re-sampling a Maxwellian distribution. From an initial normalized Maxwellian velocity distribution function with an initial temperature of 2 eV (blue), 500 discrete particles are sampled from the velocity distribution function (histogram). A new Maxwellian velocity distribution function is fit to the discrete particle distribution (orange).

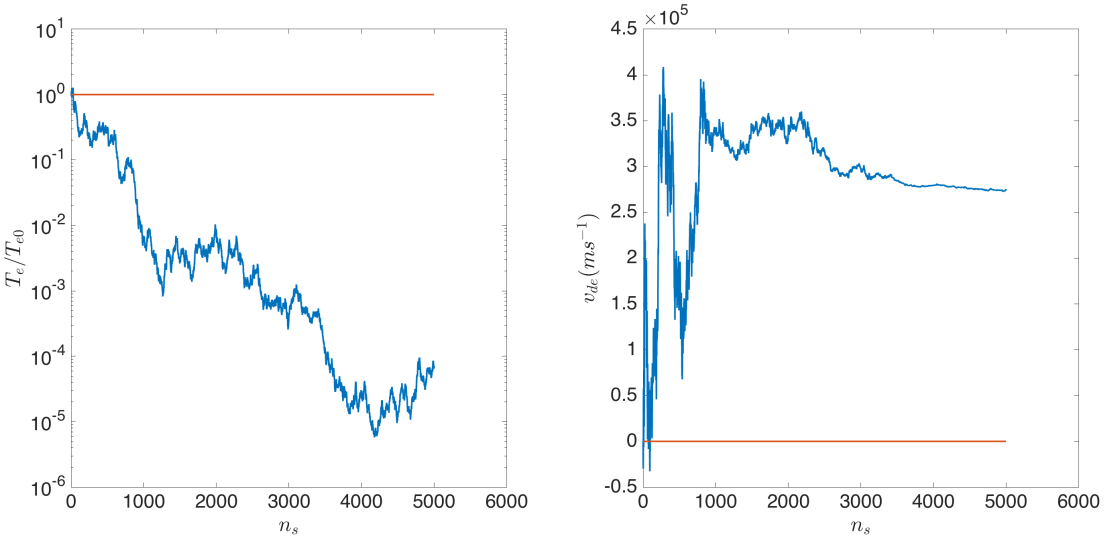

Figure 3.4: Change in the (right) electron temperature normalized by the initial temperature and (left) drift velocity as a function of number of times resampled n_s. The blue and red curve curves corresponds to the unmodified resampled distribution and distribution corrected by Eq. (3.2) respectively. The red curve is still subject to numerical precision fluctuations not visible on this scale.

CHAPTER 4

Simulation Results

Confirming the results of reference [Lafleur et al., 2016b], a strong instability is observed in our simulations when the plasma parameters in Table 3.1 are used to be qualitatively consistent with a Hall-effect thruster conditions. The baseline thruster conditions are adequate for inducing an initial beam cyclotron instability which undergoes a mode transition to an ion acoustic wave as discussed in Section 2.5. This transition occurs at approximately 0.1 μs, when the condition set by Eq. (2.27) is met. The ion acoustic wave then saturates at a quasi steady-state approximately at 2.0 μs, characterized by the trapping of ions in the electrostatic wave. The plasma then exhibits low frequency (on the order of MHz) and short wavelength (on the order of mm) fluctuations in density for each species and electric field. Even at steady state, the system is highly dynamic. The simulations show significant changes in observable quantities such as species temperatures and electrostatic wave energy (on the order of KHz).

In Section 4.1, we show the beam cyclotron instability is insufficient for producing the anomalous transport measured in experiments. The transition to the ion acoustic wave is, however, important for correctly modeling the electron cross magnetic field transport and can provide orders of magnitude additional mobility, particularly in the limit of low neutral pressures. In Section 4.2, we discuss the linear and nonlinear regimes of instability growth, modifications to the initial ion temperature and drift velocity from the baseline operating conditions and the effects on the transition to an ion acoustic wave. Evidence is then presented for a low frequency ionization fluctuations due to Landau damping oscillations in Section 4.3 which may provide an explanation for azimuthal spoke modes observed experimentally. Lastly, preliminary results for the moment method described in Section 3.4 are presented

and the possibility of resolving these instability with a fluid description is discussed.

4.1 Anomalous Mobility

In order to make use of Eq. (2.34) for calculating the anomalous mobility, we must determine the averaging quantity $\langle n_e E_y \rangle$ from our simulations. From Eq. (2.35), this averaging should be done over at least a wave period and wavelength. In Figure 4.1 and 4.2 we present the spacial-temporal variation of the normalized electron density n_e and the azimuthal electric field E_y. Immediately we may notice large fluctuations in both density (70% of n_0) and electric field (1000% of E_0). Though difficult to determine qualitatively, the fluctuations in n_e and E_y are not completely out of phase. Instead, they are correlated and the product of the two quantities is shown in Figure 4.3. The anomalous mobility can be determined from Figure 4.3 and Eq. (2.35) by averaging in space over L_y and in time from $2 - 8\mu s$. Similarly, the mobility determined from the ion density in Figure 4.4, 4.5 and Eq. (2.37) can be calculated, averaging over the same region of space and time. Lastly, the mobility is also determined using Eq. (2.39) by averaging the axial velocity for all particles. These measurements of anomalous mobility are presented in Table 4.1.

From Figure 4.6, we can extrapolate the contribution of the wave to the total cross field electron transport using expressions for electron-neutral momentum exchange cross sections given in [Goebel and Katz, 2008]. In regions of low neutral density similar to that of a the Hall-effect thruster the wave behavior can have a significant contribution to the total cross field electron transport. As the neutral density increases, the classical mobility given by Eq. (2.33) increases as well and the mobility becomes collision dominated. We should note that this approximation does not include the damping of the wave due to collisions. We would expect the mobility given by Eq. (2.34) to decrease proportionally to the neutral collision rate due to this damping. In Figure 4.7 we present the electron mobility averaged in space and plotted as a function of time using each of the three methods. The mobility determined using $\langle n_e E_y \rangle$ and $\langle n_i E_y \rangle$ are nearly identical while the mobility determined from Eq. (2.39) has comparable behavior while fluctuating significantly more. This discrepancy is

also made obvious in Table 4.1 where the average mobility $\mu_{(v_z/E_z)}$ is noticeably larger then either $\mu_{\langle n_e E_y \rangle}$ or $\mu_{\langle n_i E_y \rangle}$. The electron stream boundary condition in the axial direction may provide an explanation. Near the cathode, electrons can only complete up to half a cyclotron orbit before interacting with the boundary condition, at which point the electron is then reintroduced at the anode. In Figure 4.8, we can see a preferentially negative v_z and positive v_y for the electrons near the $z = 0$ boundary which we expect is a contributing factor to the discrepancy. A solution to this behavior has not been implemented, however, we propose for the future a streaming boundary condition which acts on the electrons when the guiding center interacts with the boundary condition, thereby retaining the full cyclotron behavior of the electron near the boundary. We also expect the different methods to converge when increasing the channel length L_{ch}. As a whole, the results we have obtained for the mobility and field configurations at steady state are consistent with reference [Lafleur et al., 2016b].

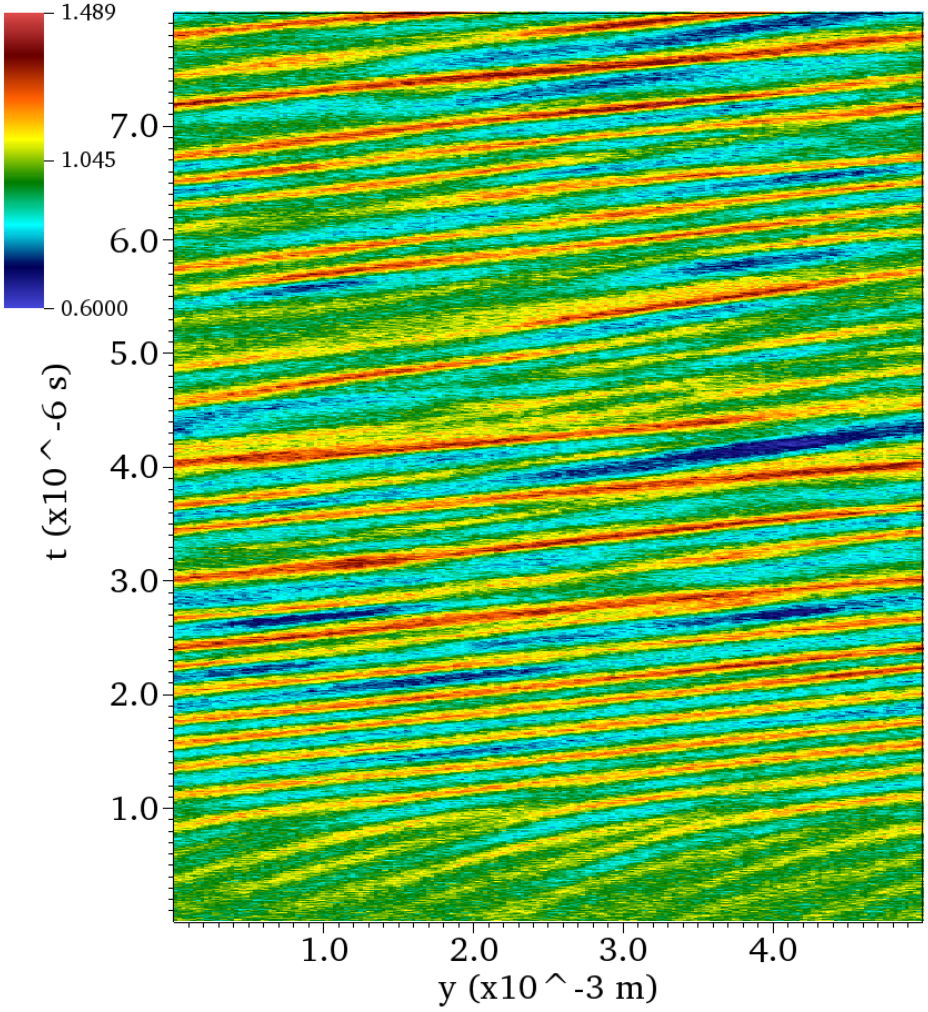

Figure 4.1: Contour plots of the spatial-temporal variation of the electron density n_e normalized by the initial plasma density used in the initial condition ($n_0 = 1e17$). The electron density begins to exhibits high-frequency (of the order of MHz) and short-wavelength (of the order of mm) fluctuations at approximately 2.0 μs. The estimated the wave parameters show good agreement with analytical values for the ion acoustic wave.

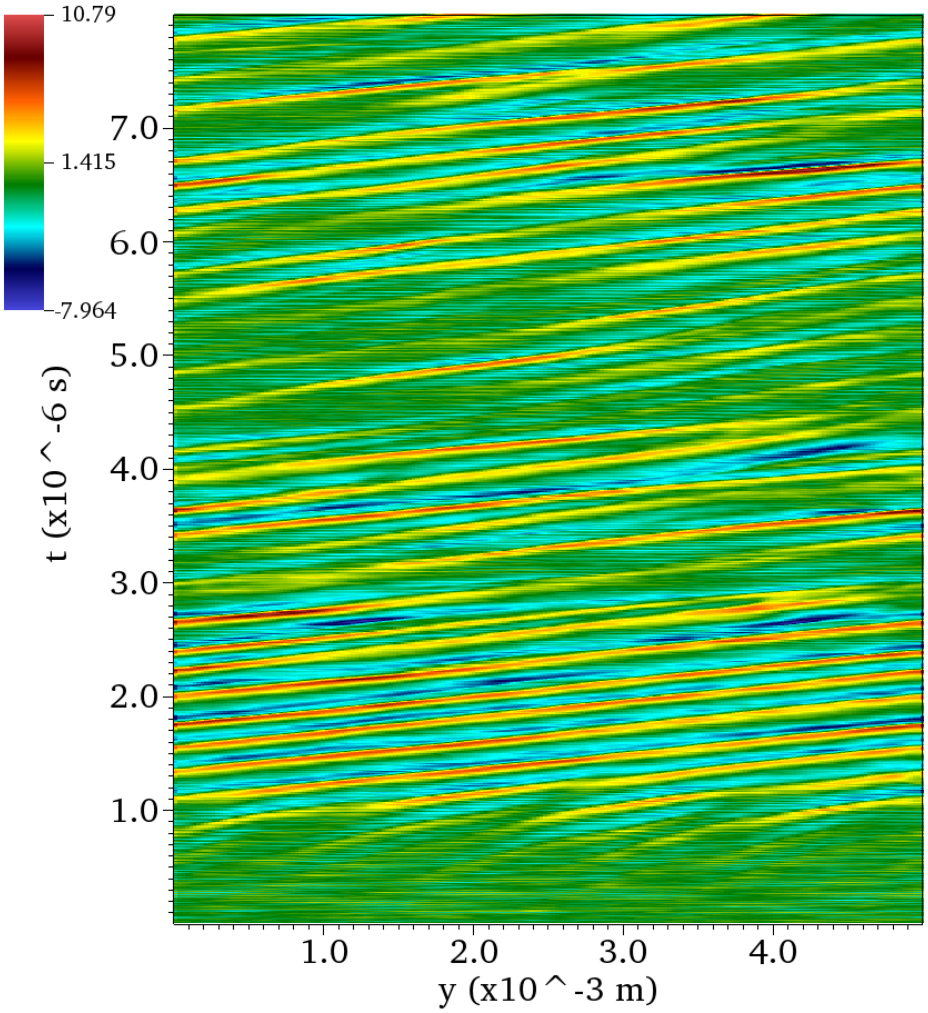

Figure 4.2: Contour plots of the spatial-temporal variation of the azimuthal electric field E_y normalized by the imposed electric field along the channel ($E_0 = 20000\ V$). The electric field begins to exhibits high-frequency (of the order of MHz) and short-wavelength (of the order of mm) fluctuations at approximately 2.0 μs. The estimate of the wave parameters show good agreement with analytical values for the ion acoustic wave.

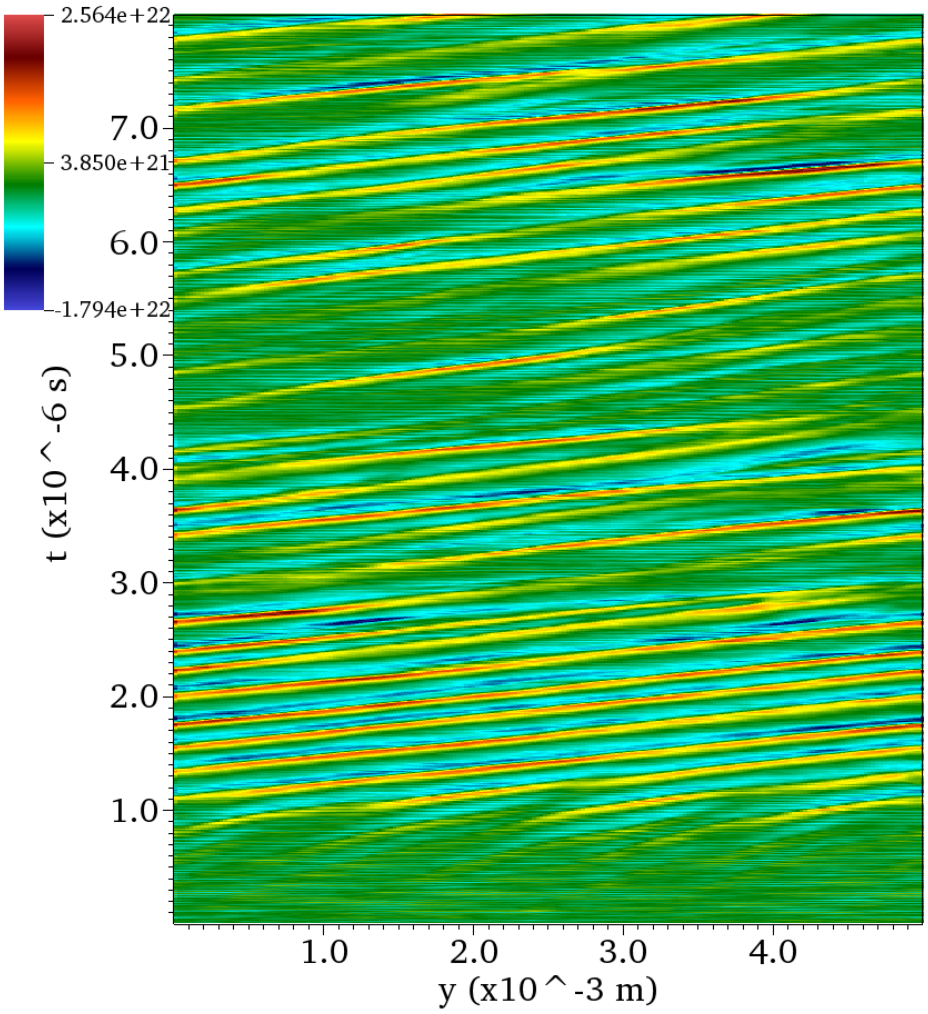

Figure 4.3: Contour plots of the spatial-temporal variation of the electron density multiplied by the azimuthal electric field $n_e(y,t)E_y(y,t)$.

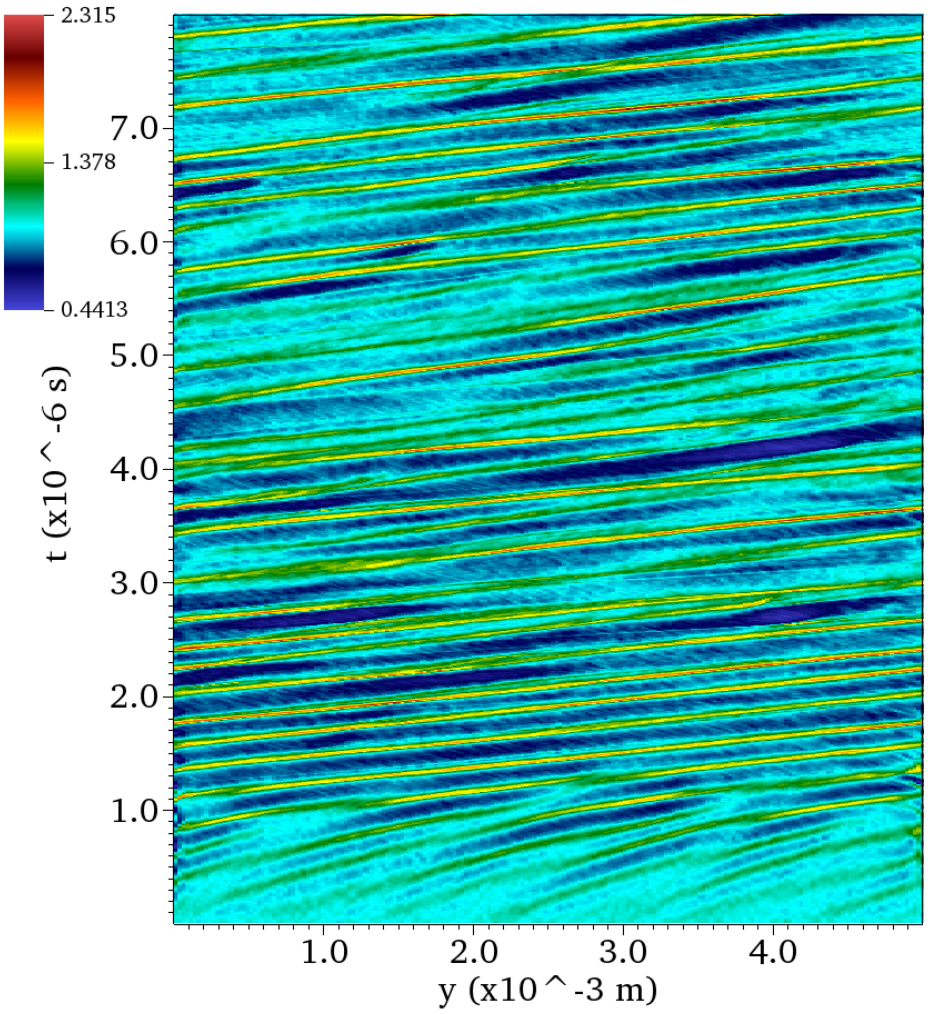

Figure 4.4: Contour plots of the spatial-temporal variation of the ion density n_i normalized by the initial plasma density used in the initial condition ($n_0 = 1e17$). The ion density begins to exhibits high-frequency (of the order of MHz) and short-wavelength (of the order of mm) fluctuations at approximately 2.0 μs. The estimate of the wave parameters show good agreement with analytical values for the ion acoustic wave.

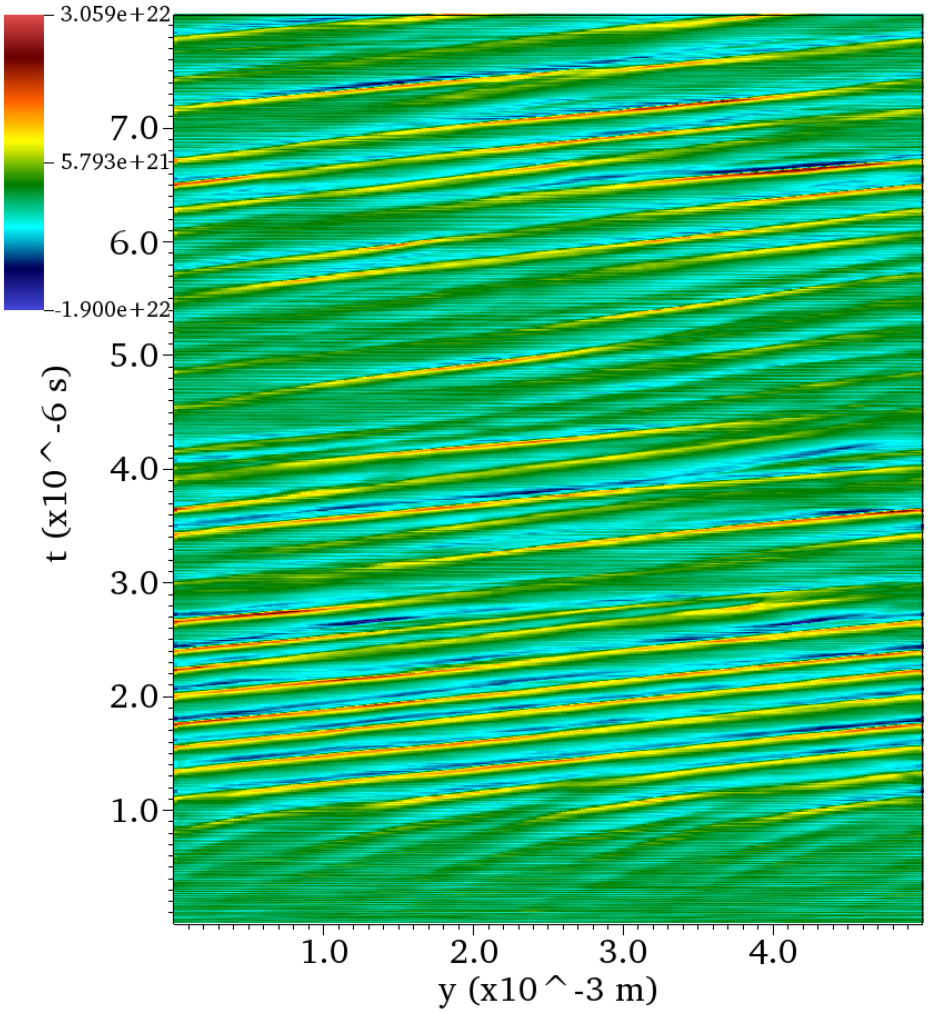

Figure 4.5: Contour plots of the spatial-temporal variation of the ion density multiplied by the azimuthal electric field $n_i(y,t)E_y(y,t)$.

Instability Property (Full Kinetic)	Value
$\mu_{\langle n_e E_y \rangle}$ $(m^2 V^{-1} s^{-1})$	3.7225
$\mu_{\langle n_i E_y \rangle}$ $(m^2 V^{-1} s^{-1})$	3.6950
$\mu_{(v_z/E_z)}$ $(m^2 V^{-1} s^{-1})$	4.2590

Table 4.1: Averaged cross field mobility due to the ion acoustic wave calculated with three different methods for simulation using baseline operating conditions between $2 - 8$ μs.

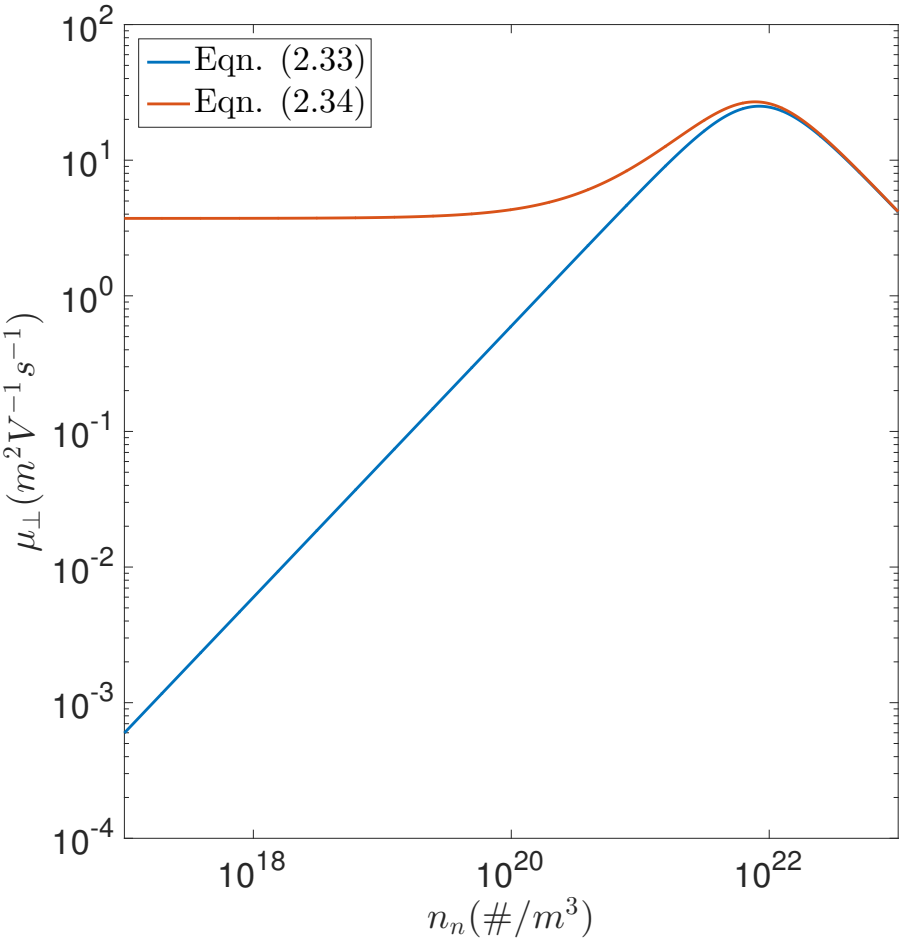

Figure 4.6: Utilizing electron-neutral momentum exchange cross sections presented in [Goebel and Katz, 2008], a total electron cross field mobility is approximated using $\mu_{\langle n_e E_y \rangle}$ from Table 4.1 in the presence of collisions as a function of neutral number density n_n.

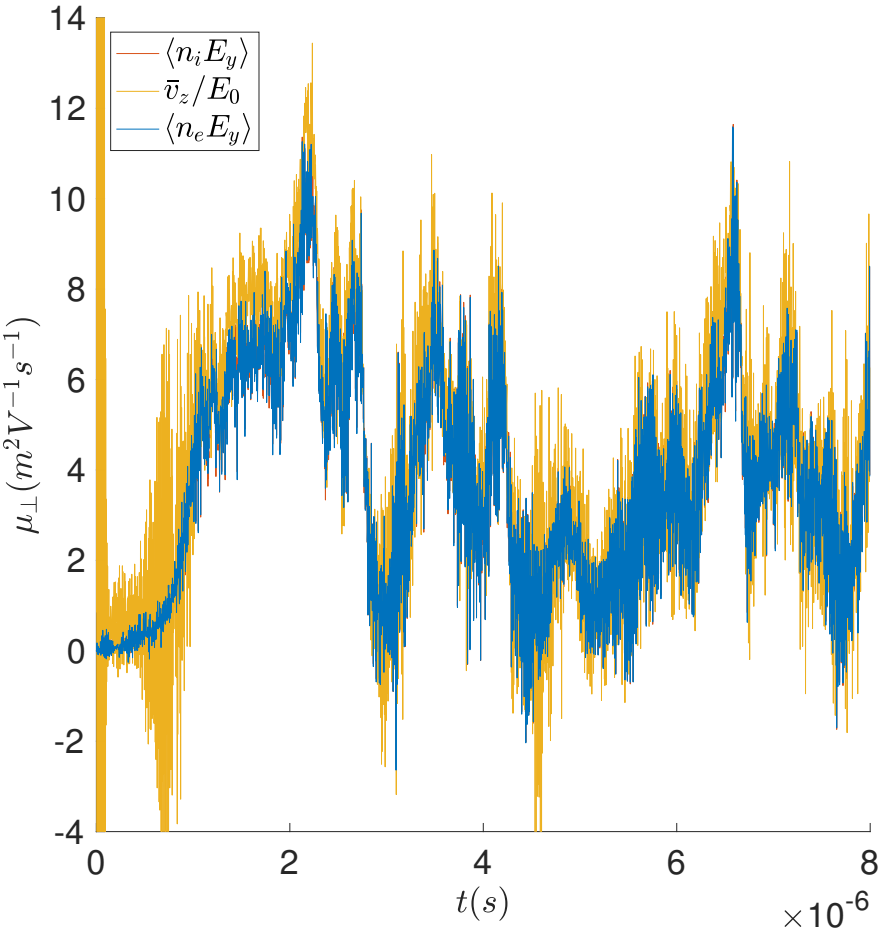

Figure 4.7: Spatially averaged mobility as a function of time utilizing the three different methods outlined in Section 2.6.

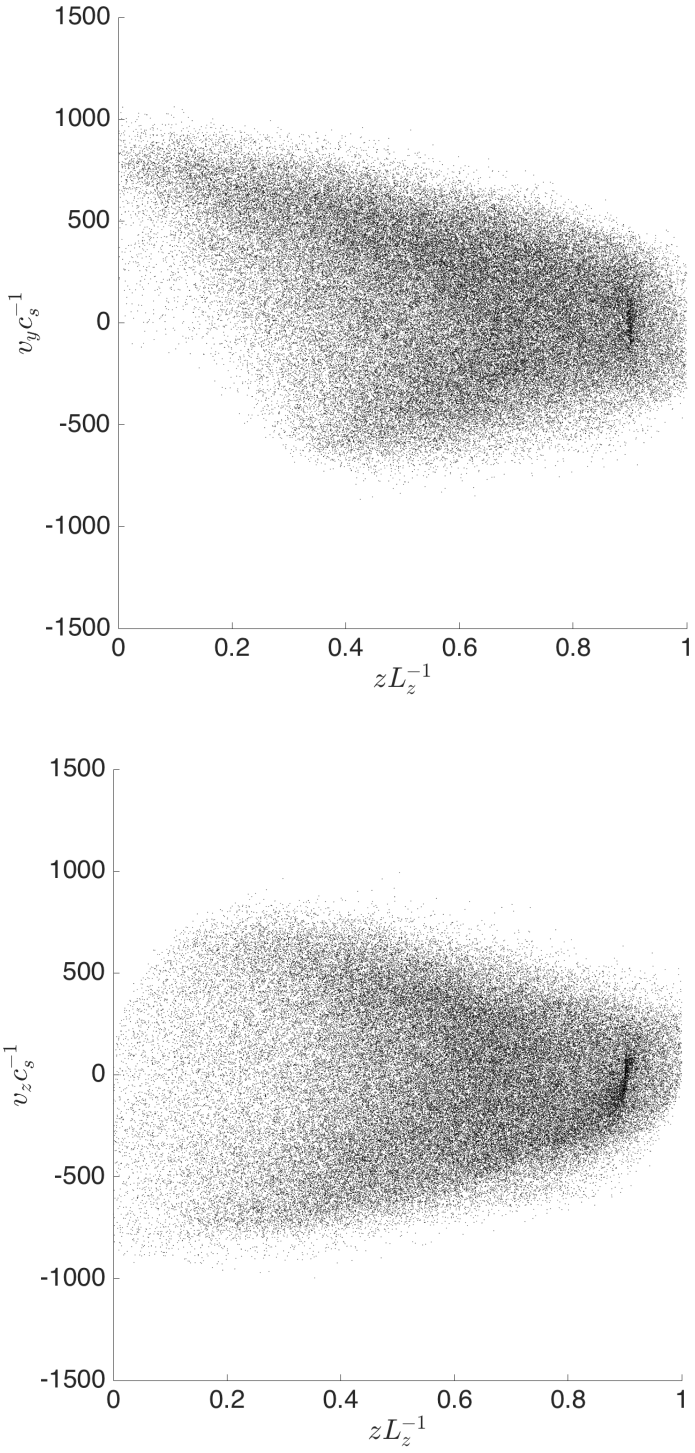

Figure 4.8: Electron phase space with (top) azimuthal and (bottom) axial velocity normalized by the sound speed as a function of axial position normalized by the channel length L_{ch} at $t = 2.5\mu s$.

4.2 Instability Formation and Steady-State Behavior

In order to integrate a theory for the anomalous cross field electron mobility with Hall-effect thruster simulations, an understanding of the nonlinear instability evolution is essential. In Figure (4.9) we show the azimuthal temperature for both species and the electrostatic wave energy as a function of time for the baseline operating conditions. It is important to note that the distribution functions for both species can be non-Maxwellian, in which case, the temperature simply acts as a method of measuring the standard deviation in velocity. To illustrate this, we also show phase space, and distribution functions for each species at different points of interest labeled with (a), (b), (c), (d), and (e) in Figure 4.10, 4.11, 4.12, 4.13, and 4.14 respectively.

Upon inspection of Figure 4.9 we see an initial growth within 0.1 μs of the simulation. This region of linear growth is the beam cyclotron instability and occurs on a time scale much shorter than the ions. In Figure 4.10 we see electron trapping and resonance broadening analogous to what is presented by [Davidson, 1972]. The centroid of the electron phase space loops can be used to approximate the phase velocity of the beam cyclotron instability $v_p \approx v_d$. This is consistent with our analysis in Section 2.2. The electrons are then heated to approximately 10 eV with a corresponding thermal velocity of $v_{T_e} \approx v_d$. This represents a *knee* in the instability growth and the beam cyclotron instability saturates due to electron Landau damping. This *knee*, given by Eq. (2.27), occurs at a critical amplitude of the turbulent fields. [Lampe et al., 1971] argues that due to the presence of magnetic fields, longtime trapping of electrons in a large amplitude coherent wave does not occur, instead the electron distribution relaxes to a state resembling a Maxwellian distribution soon after.

Simultaneously, the ions start to partake in the instability and the development of an ion acoustic wave begins. The electrons are heated to $v_{T_e} \gg v_d$ as predicted in reference [Lampe et al., 1971] and the electrostatic field energy increases as the ion density gradients grow. It is in Figure 4.11 where we begin to see the onset of ion trapping (the mechanism which the ion acoustic wave will saturate) and a thermalized electron distribution function which is approximately Maxwellian. When the ion temperatures reach a peak at approx-

imately $t = 2.5\ \mu s$, the ion acoustic wave is considered saturated. Figure 4.12 shows the ion distribution as very non-Maxwellian with significant amount of ion phase space trapping. The ion velocity distribution function resembles that of a bump-on-tail discussed in [Krall et al., 1974]. We have determined it is at approximately this time when it is appropriate to begin sampling the steady state mobility properties discussed in Section 4.1. As predicted in Section 2.2 and 2.3, the growth rate of the beam cyclotron instability is significantly larger than the ion acoustic wave and similar to the analysis done in Section 2.2 and 2.3. The centroid of the ion phase space loops in Figure 4.12 can also be used to approximate the phase velocity of the ion acoustic wave, $v_p \approx \sqrt{\frac{2}{3}} c_s$.

From Figure 4.9 it is obvious there are large fluctuations in species temperature and wave energy even at saturation. When the ion temperature is large enough for a significant portion of the ion velocity distribution function to interact with the wave at a phase velocity v_p and the stability criterion, approximated by Eq. (2.28), is easily met, the ion acoustic wave becomes ion Landau damped. This damping is significant enough to decrease the temperature of both species and wave energy until the criteria for stability is no longer met. The ion velocity distribution function then undergo periodic behavior of growth and damping as shown in Figure 4.13 and 4.14. This periodic behavior is also made obvious in the magnitude of waves shown in Figure 4.3 and the electron mobility in Figure 4.7 which all oscillate at approximately the same frequency on the order of KHz. As a result, the ion acoustic wave is highly dynamic even at saturation and averaging of the mobility should be made over multiple periods of this Landau oscillation to be statistically significant. Further work should be performed to verify whether the results presented in this work for the anomalous mobility are averaged over a large enough region in time.

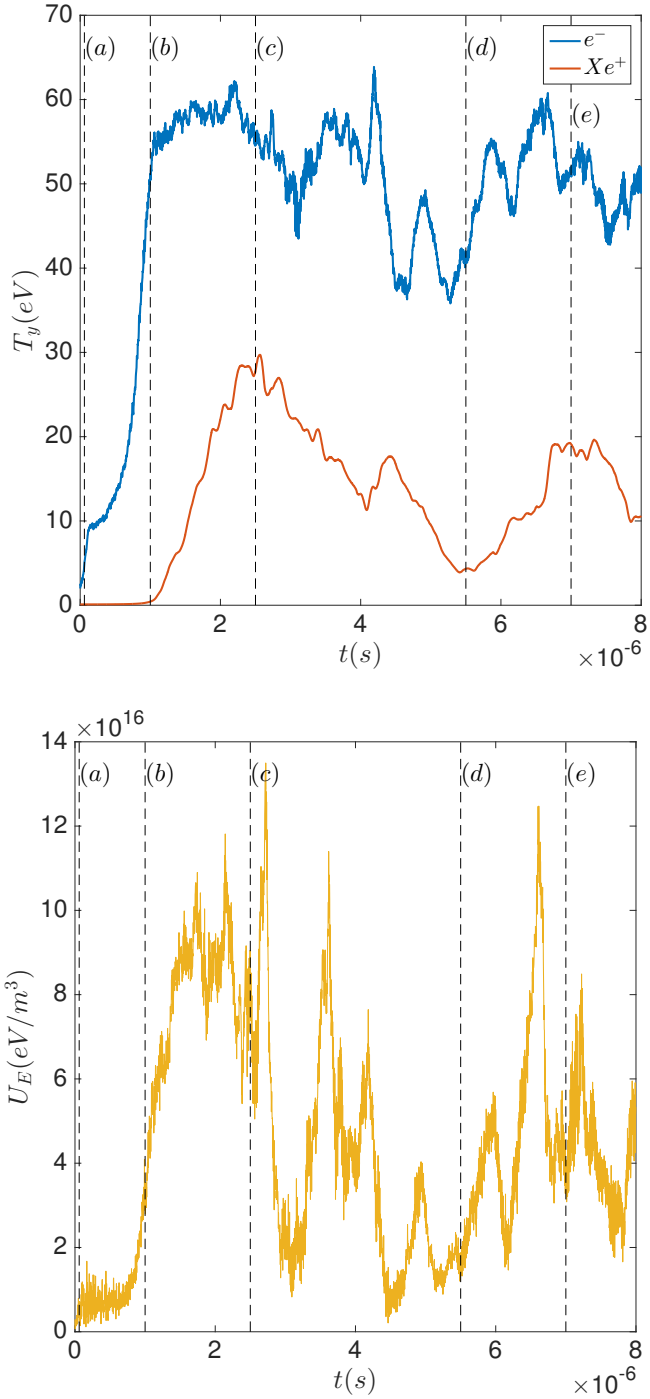

Figure 4.9: (Top) Spatially average azimuthal temperature as a function of time for both electrons and ions in electron volts. The time positions (a), (b), (c), (d), and (e) correspond to phase space in the following plots. (Bottom) Spatially averaged electrostatic wave energy as a function of time. Similar behavior can be seen between the electron thermal energy and electrostatic wave energy. Both figures are for baseline operating conditions.

4.2.1 Condition for Mode Transition to Ion Acoustic Wave

A brief parametric study is also conducted comparing temperature and velocity ratios similar to the work presented in [Lampe et al., 1971]. In the context of a Hall-effect thruster, we show the same stability criteria apply to the velocity and temperature ratios. In Figure 4.15, we show the stability criterion Eq. (2.28) is sufficient for determining whether a transition to an ion acoustic wave will occur. Modifications of the initial temperature ratio and velocity ratio are performed by adjusting the ion temperature and the externally applied magnetic field in Table 3.1 respectively. When the stability criterion is met, the plasma saturates after the beam cyclotron instability and no mode transition occurs. In previous sections we have argued that the beam cyclotron instability is insufficient in producing enough anomalous cross field electron transport and that the ion acoustic wave is necessary. Simulations of Hall-effect thruster channels using HPHall have shown the region most likely to produce this anomalous mobility is near the channel exit where the external fields have the highest magnitude and the neutral density (and electron neutral collisions) are the least significant. Future work is suggested to confirm this result and investigate the effect of ion acoustic wave in the plume region of a Hall-effect thruster where a significant amount of anomalous electron transport is required.

4.2.2 Frozen Ion Distribution Function

For the purpose of investigating the possibilities of a reduced order simulation, a numerical experiment is conducted where the ion distribution is frozen in time at point (c) of Figure 4.9. In Figure 4.12, we observe large density perturbations in the ion spatial distribution function. As expected, when the electrons are allowed to evolve in time with a frozen ion distribution, the electron mobility remains constant. The average electron mobility is determined to be $\mu_{\langle n_e E_y \rangle} = 6.4720\ m^2 V^{-1} s^{-1}$ with a standard deviation of $\sigma_\mu = 1.0180\ m^2 V^{-1} s^{-1}$, consistent with Figure 4.7. The mobility produced with the frozen ion distribution function is shown in Figure 4.16. Furthermore, retaining the ion distribution function and initializing the electrons as a cold Maxwellian and uniform in position (identical to the initial condition given in Table 3.1) produces the same mobility after the brief beam-cyclotron instability transition shown in Figure 4.17. When a similar procedure is conducted at the simulation times denoted by (d) and (e) in Figure 4.9, we observe consistent behavior. Assuming we can accurately predict the wavelength and amplitude corresponding to the ion acoustic wave for a given Hall-effect thruster state, an approximation of the ion density oscillations may be useful for quickly determining the anomalous electron mobility on time scales shorter than the ion landau damping oscillations.

4.3 Low Frequency Ionization Fluctuations

Observations of an azimuthally rotating oscillation with an angular frequency in the tens to hundreds of kHz band has been recently published by a number of authors including [McDonald and Gallimore, 2011], [Sekerak et al., 2013], and [Cunningham et al., 2016]. This is frequently referred to as a spoke mode by the experimental community and has been characterized by high speed imaging, emissive probe measurements, and magnetic sensing of Hall current. Figure 4.9 has shown that at saturation, our simulation undergoes large fluctuations of electron and ion temperature on the order of $10 - 20\ eV$. Cross sections for collisions between electrons and ground state Xe presented by Chung et al. (2005) show an expected 10% increase in ionization due to the electron temperature oscillations alone. Though we could not find ionization rates for collisions between $Xe+$ and ground state Xe, we do not expect the oscillations in ion temperature to be negligible either. A similar analysis will show significant fluctuation in the Xe radiative power rates due to the same Landau oscillations. With this information, an indirect comparison can be made between the work presented here and visible plasma emission due to azimuthal spokes presented in Cunningham et al. (2016). Video light intensity measurements at a single azimuthal position in the Hall-effect thruster demonstrate a breathing mode oscillation with a period of approximately 70 μs and a spoke mode with a period of 5 μs. A comparison can not be made between the ion acoustic wave frequency (on the order of MHz) in these experimental measurements due to the temporal resolution of the cameras, however, a comparison between the spoke mode frequency and Landau damping oscillation frequency shows they are in good agreement. These Landau damping fluctuations provide a reasonable order of magnitude explanation for the spoke modes observed experimentally and further investigation is suggested.

4.4 Electron Moment Method

To complete this chapter, we present a preliminary study of electron moment method implemented with our baseline simulation operating conditions. As expected, the electron cyclotron beam instability is no longer resolved due to the inability to capture kinetic effects (i.e. trapping) of the electrons. Instead, the electrons are immediately heated to approximately 100 eV within the first 0.1 μs and little variation in the temperature is seen over time. This is of course, inconsistent with our full kinetic simulations. The ion acoustic wave growth rates are smaller than the full kinetic cases shown previously, however, in Figure 4.18, 4.19, and 4.20 we still observe the characteristic density and electric field fluctuations approximately 3.5 μs into the moment method simulations. The electron cross field mobility are determined and compared to the full kinetic simulations with baseline operating conditions and presented in Table 4.2. When averaging over a region of time where the electron moment method ion acoustic wave is saturated, the electron mobility is significantly reduced compared to the full kinetic simulations. Despite producing waves with features qualitatively comparable to the full kinetic simulations, upon closer inspection, the plasma appears to be heavily damped numerically and the measurable quantities of the plasma disagree with the electron mobility in our baseline cases shown in Table 4.1. This suggest further investigation of the impact of finite collisionality may be useful.

Instability Property (Electron Moment Method)	Value
$\mu_{\langle n_e E_y \rangle}$ $(m^2 V^{-1} s^{-1})$	0.8255
$\mu_{\langle n_i E_y \rangle}$ $(m^2 V^{-1} s^{-1})$	0.8385
$\mu_{(v_z/E_z)}$ $(m^2 V^{-1} s^{-1})$	0.7565

Table 4.2: Averaged cross field mobility due to the ion acoustic wave calculated with three different methods for simulation using baseline operating conditions and the electron moment method.

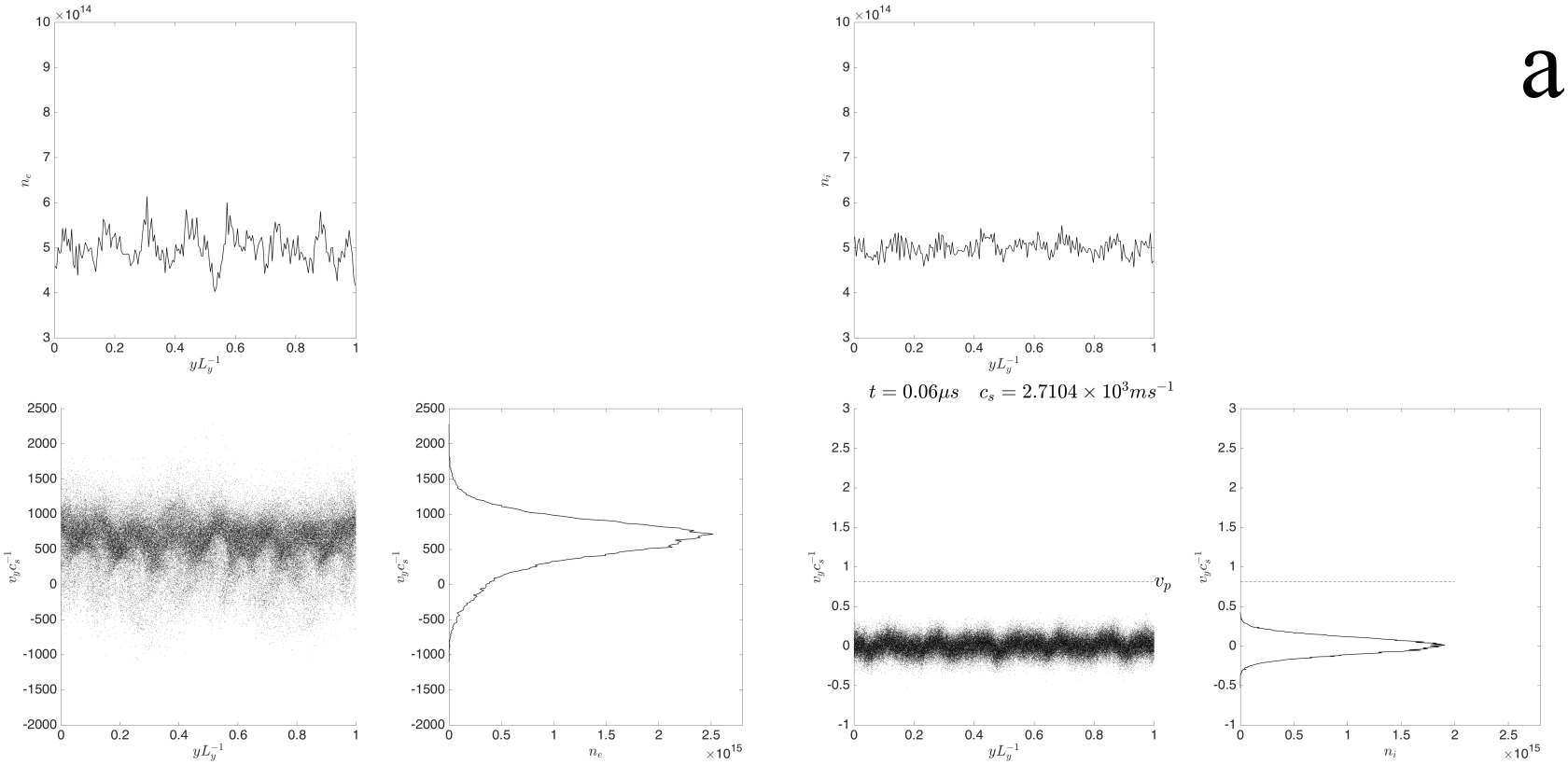

Figure 4.10: (Left) Electron and (right) ion phase space at (a) corresponding to the beam cyclotron instability. The ion acoustic phase velocity which is constant with respect to the ion sound speed is plotted for reference.

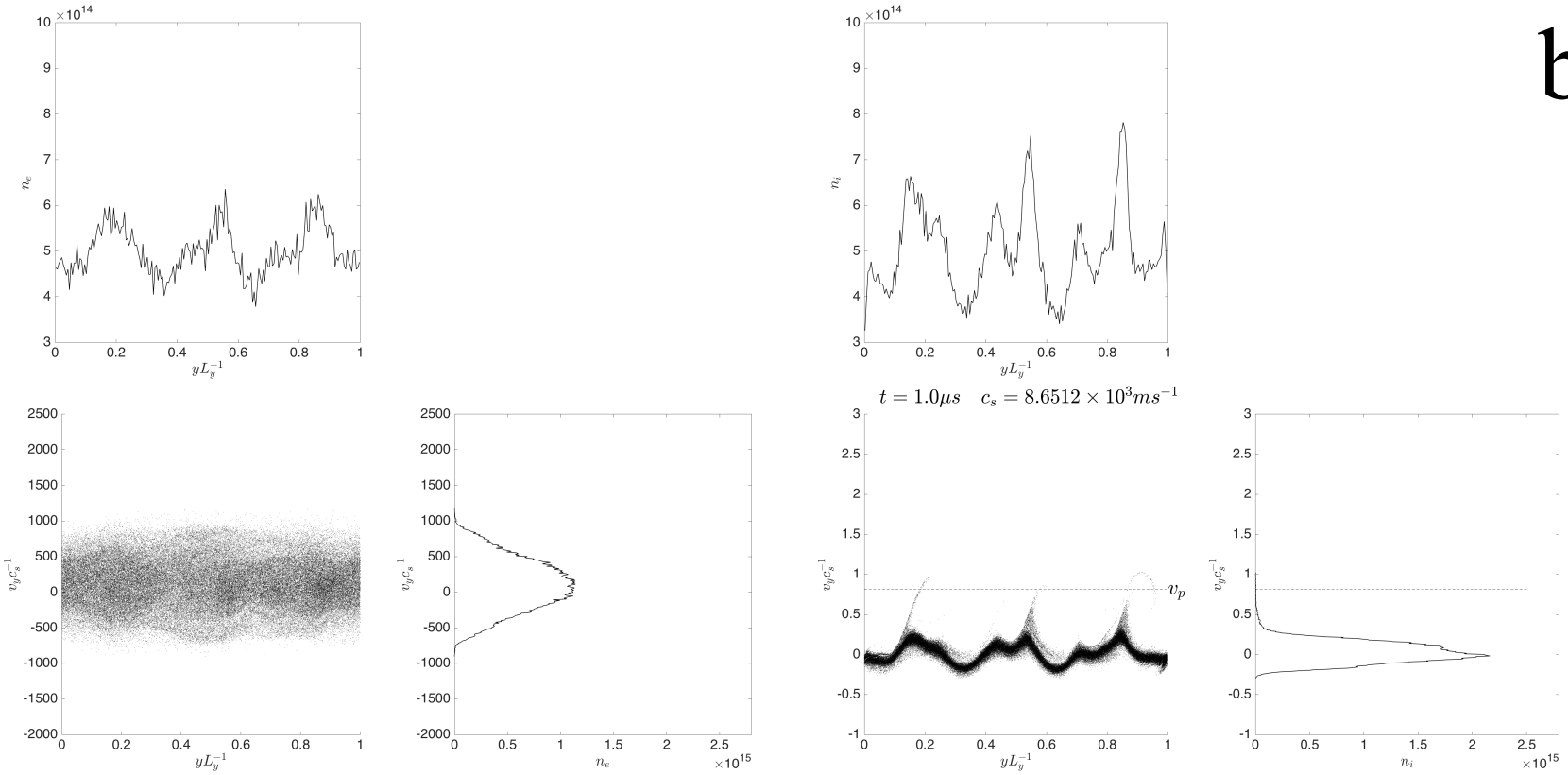

Figure 4.11: (Left) Electron and (right) ion phase space at (b) corresponding to the growth of the ion acoustic wave. The ion acoustic phase velocity which is constant with respect to the ion sound speed is plotted for reference.

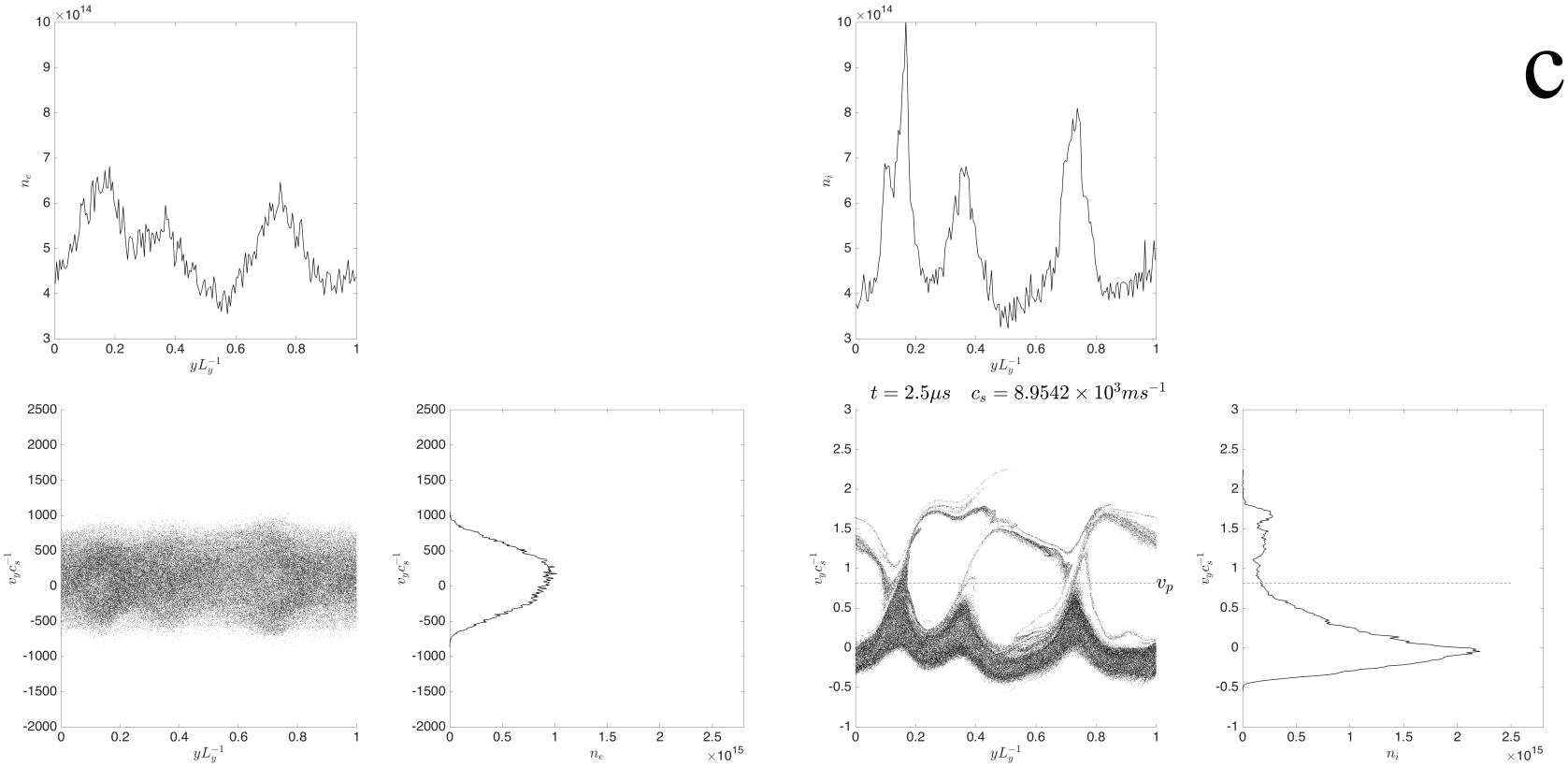

Figure 4.12: (Left) Electron and (right) ion phase space at (c) corresponding to the saturation of the ion acoustic wave. The ion acoustic phase velocity which is constant with respect to the ion sound speed is plotted for reference.

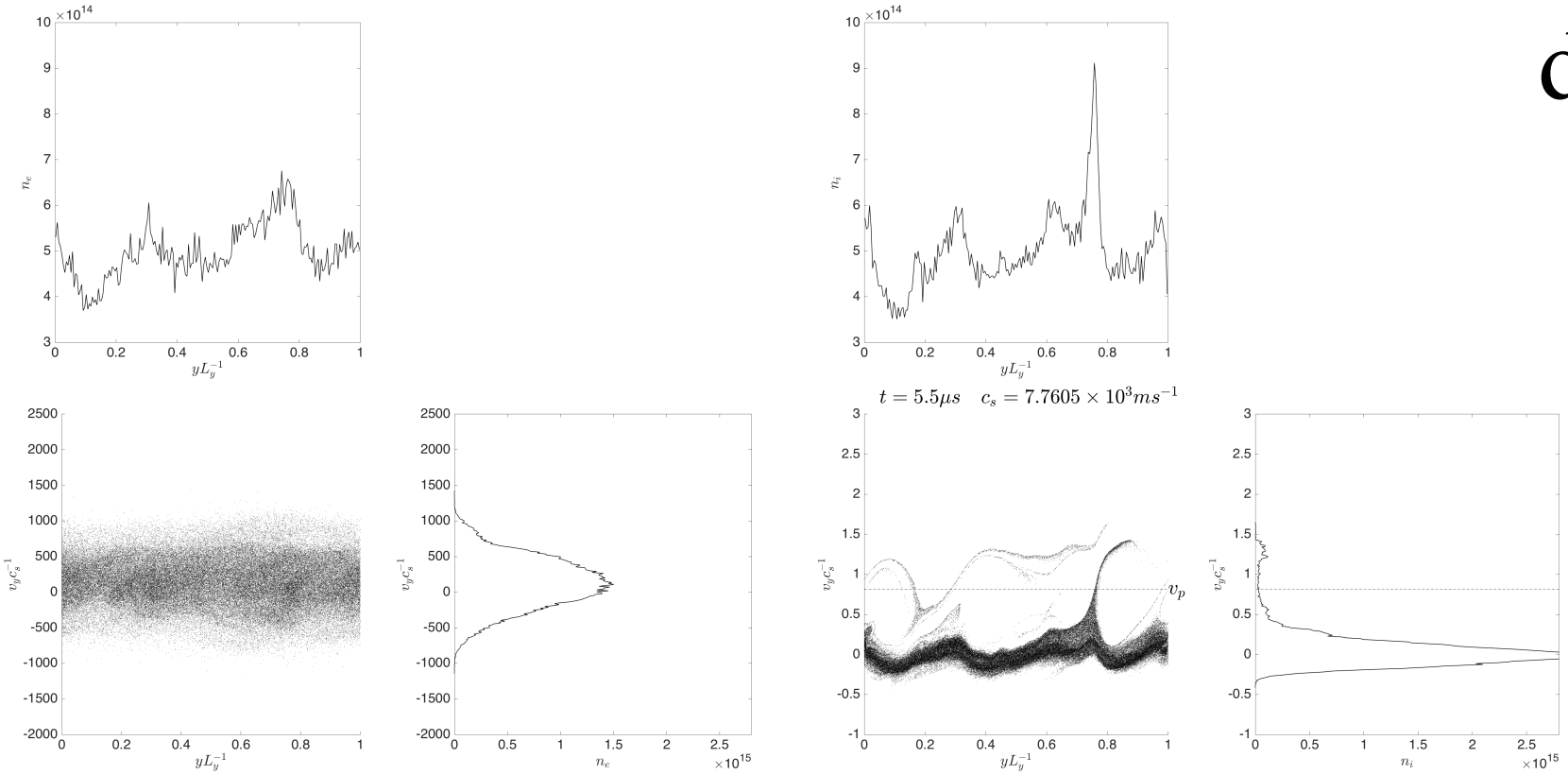

Figure 4.13: (Left) Electron and (right) ion phase space at (d) corresponding to the Landau damped ion acoustic wave. The ion acoustic phase velocity which is constant with respect to the ion sound speed is plotted for reference.

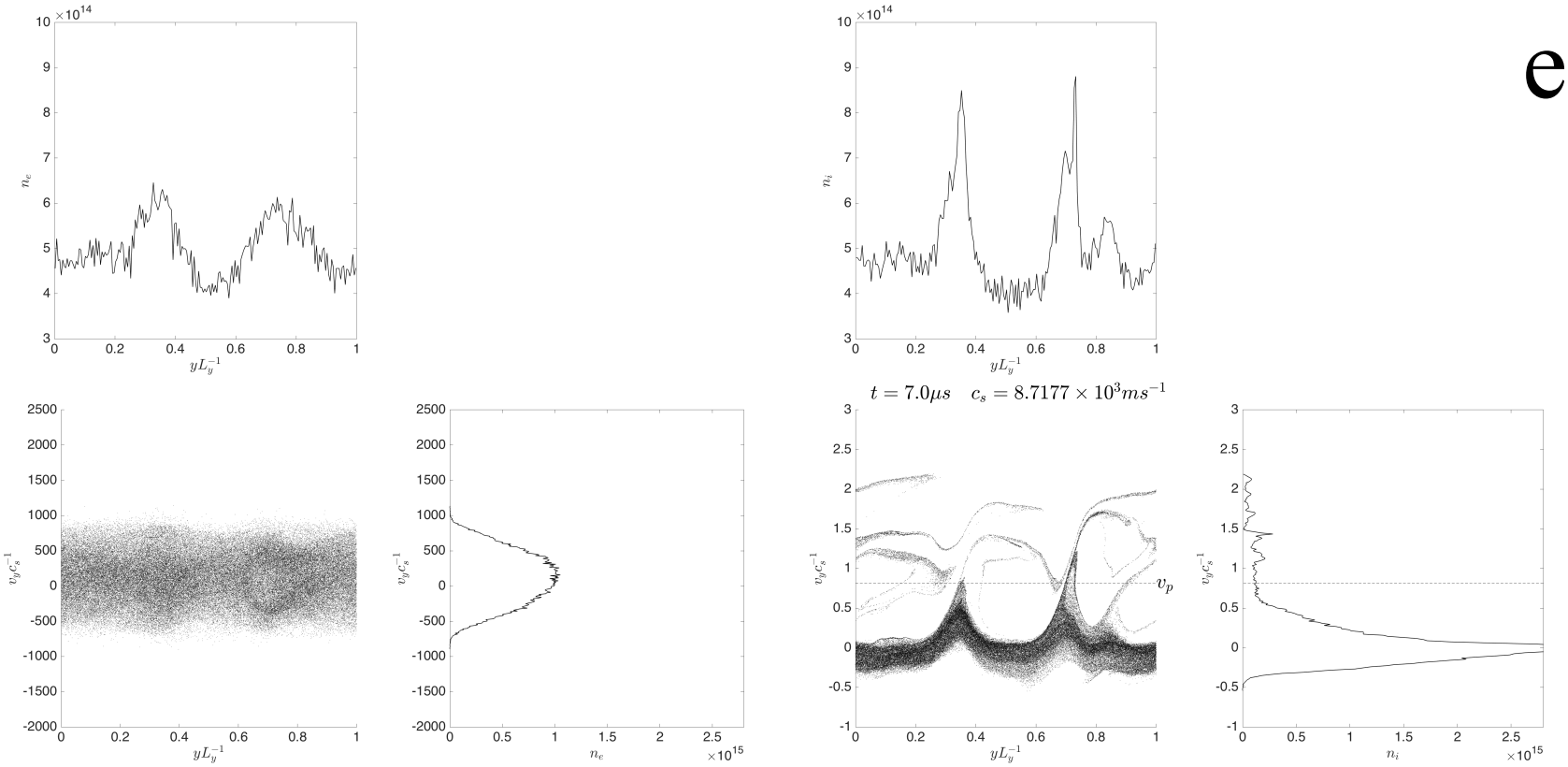

Figure 4.14: (Left) Electron and (right) phase space at (e) corresponding the second period of growth of an ion acoustic wave. The ion acoustic phase velocity which is constant with respect to the ion sound speed is plotted for reference.

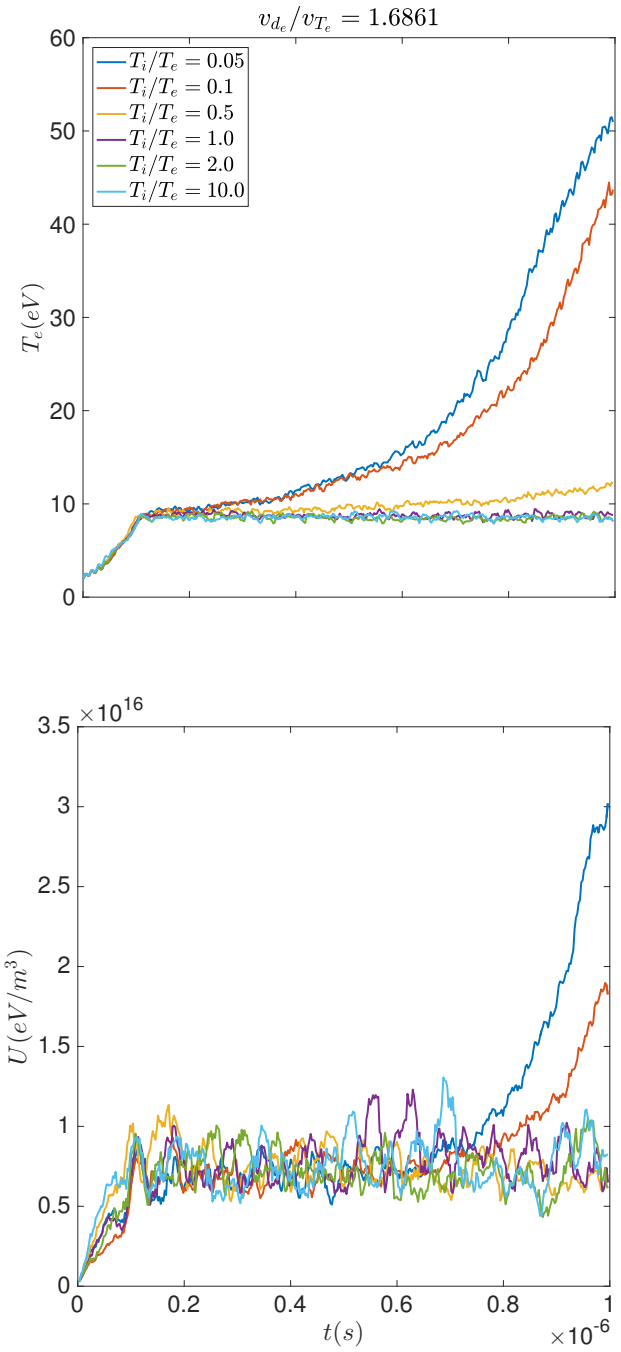

Figure 4.15: Electron temperature (top) and electrostatic wave energy (bottom) plotted as a function of time for the velocity ratio $v_{d_e}/v_{T_e} = 0.5930$ and different temperature ratios T_i/T_e at $t = 0$. Conditions where Eq. (2.28) is met do not exhibit a second phase of exponential growth (corresponding to the ion acoustic wave) after the beam cyclotron instability. Baseline operating conditions are $T_i/T_e = 0.05$.

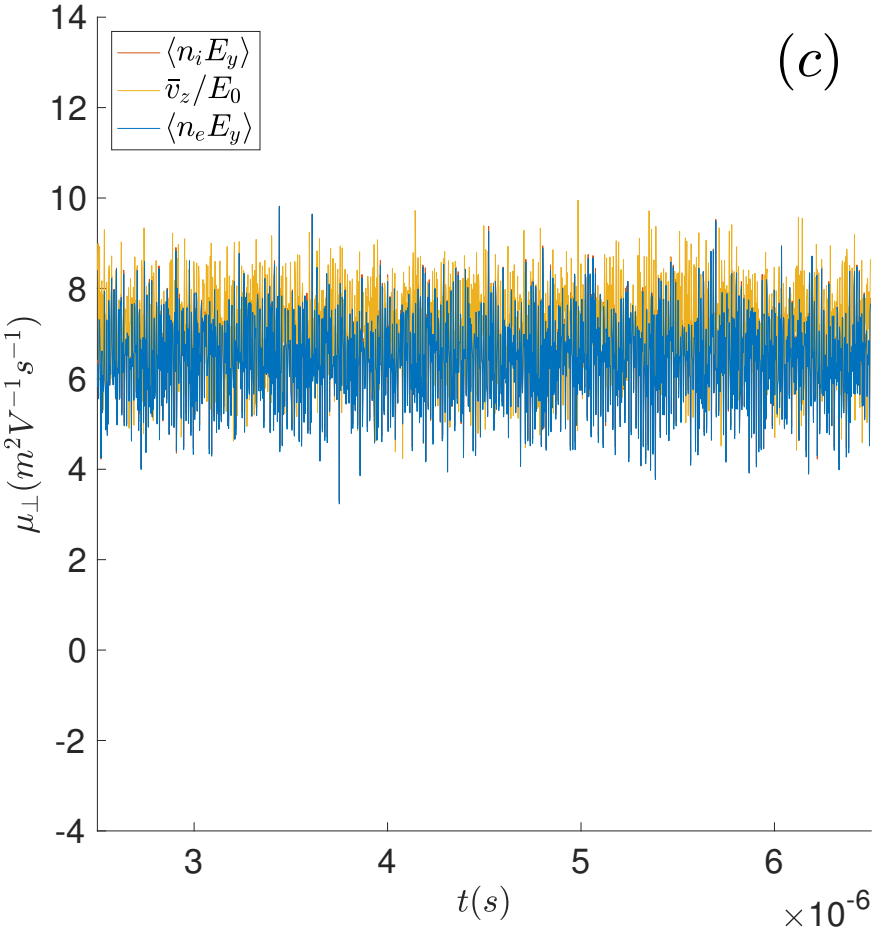

Figure 4.16: Spatially averaged mobility plotted as a function of time with frozen ion position distribution function.

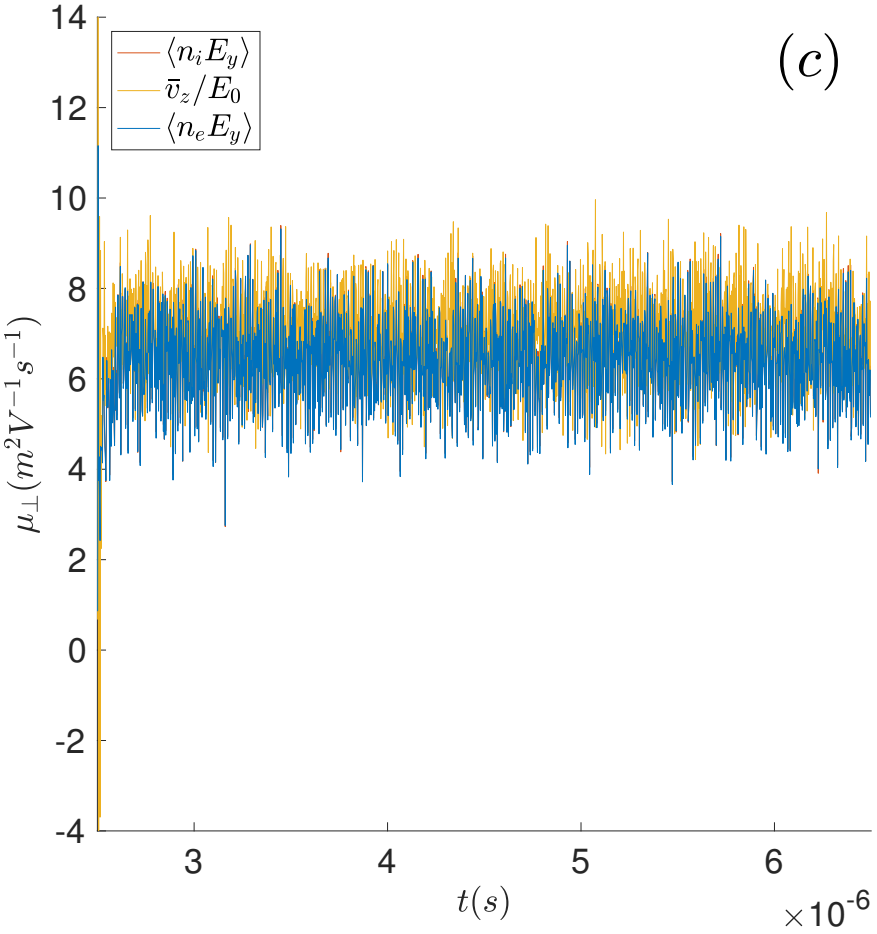

Figure 4.17: Spatially averaged mobility plotted as a function of time with frozen ion position distribution function. Electrons are initialized as a uniform cold Maxwellian.

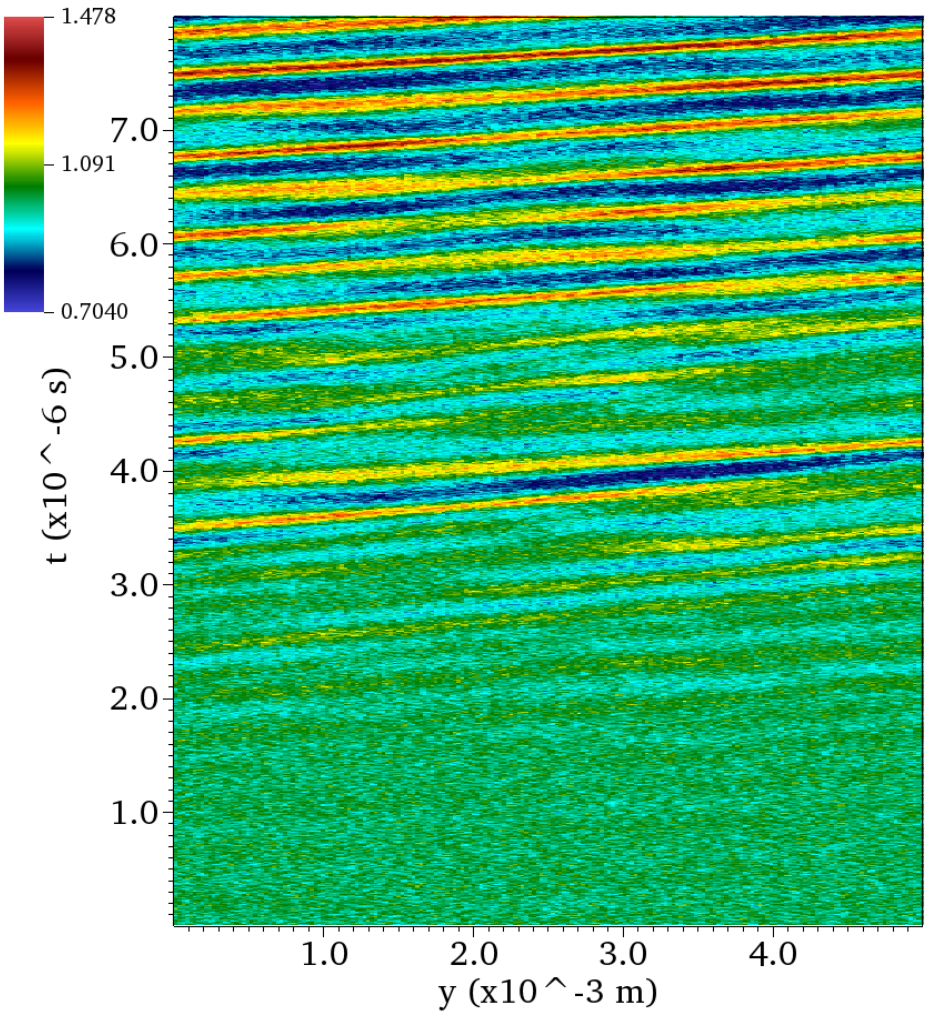

Figure 4.18: Contour plots of the spatial-temporal variation of the electron density n_e normalized by the initial plasma density used in the initial condition ($n_0 = 1e17$) for the moment electron simulations. The electron density begins to exhibits high-frequency (of the order of MHz) and short-wavelength (of the order of mm) fluctuations at approximately 3.5 μs.

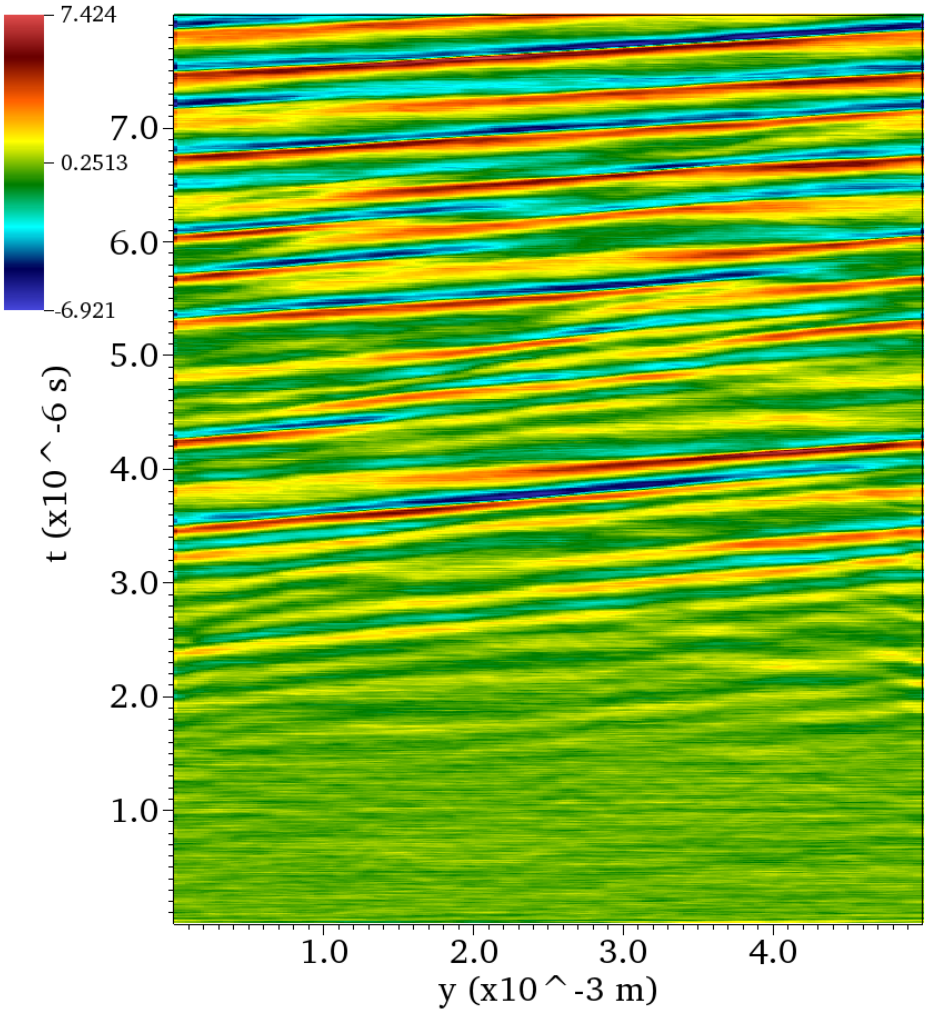

Figure 4.19: Contour plots of the spatial-temporal variation of the azimuthal electric field E_y normalized by the imposed electric field along the channel ($E_0 = 20000\ V$) for the moment electron simulations. The electric field begins to exhibits high-frequency (of the order of MHz) and short-wavelength (of the order of mm) fluctuations at approximately 3.5 μs.

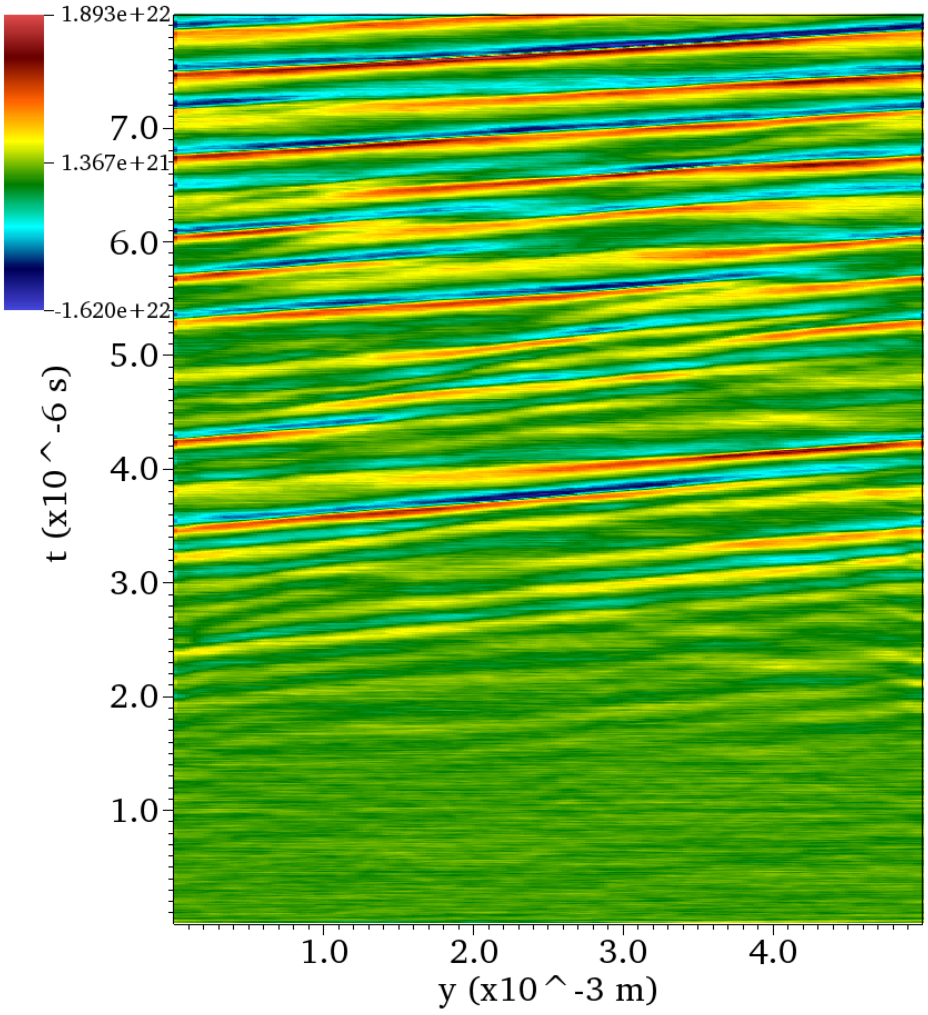

Figure 4.20: Contour plots of the spatial-temporal variation of the electron density multiplied by the azimuthal electric field $n_e(y,t)E_y(y,t)$ for the moment electron simulations.

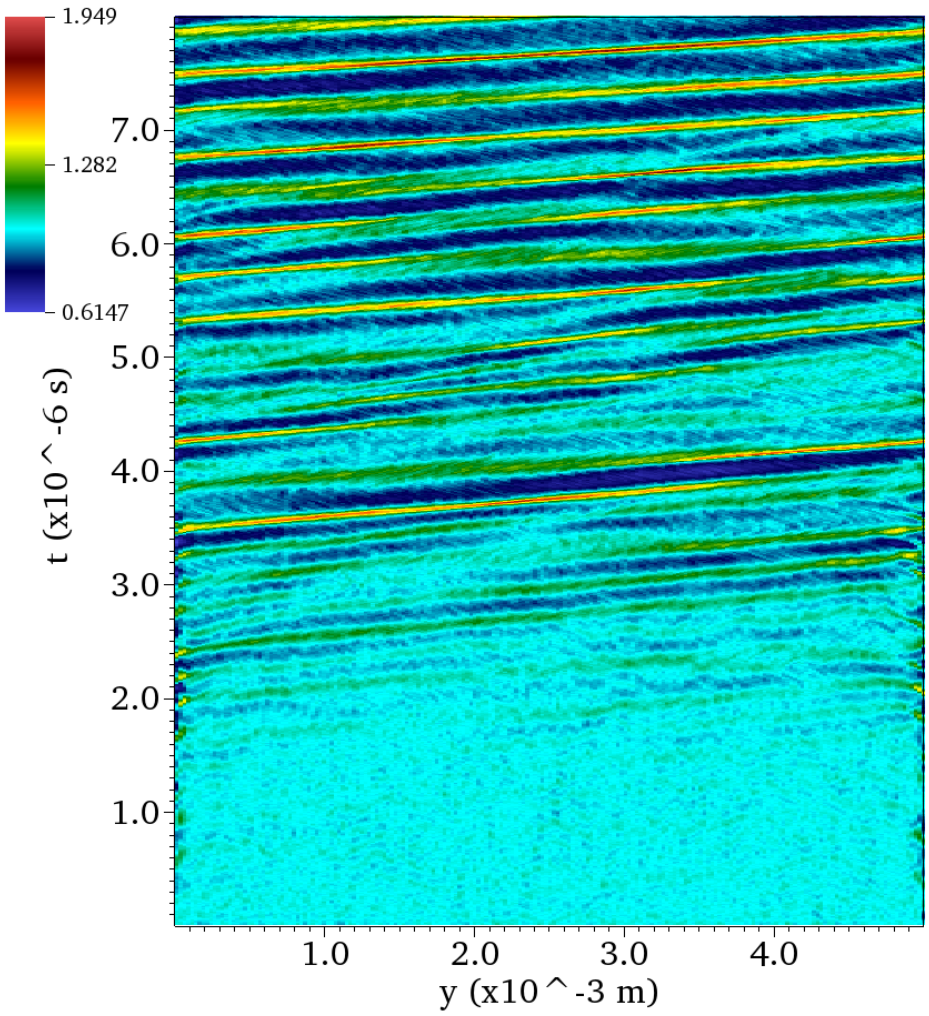

Figure 4.21: Contour plots of the spatial-temporal variation of the ion density n_i normalized by the initial plasma density used in the initial condition ($n_0 = 1e17$) for the moment electron simulations. The ion density begins to exhibits high-frequency (of the order of MHz) and short-wavelength (of the order of mm) fluctuations at approximately 3.5 μs.

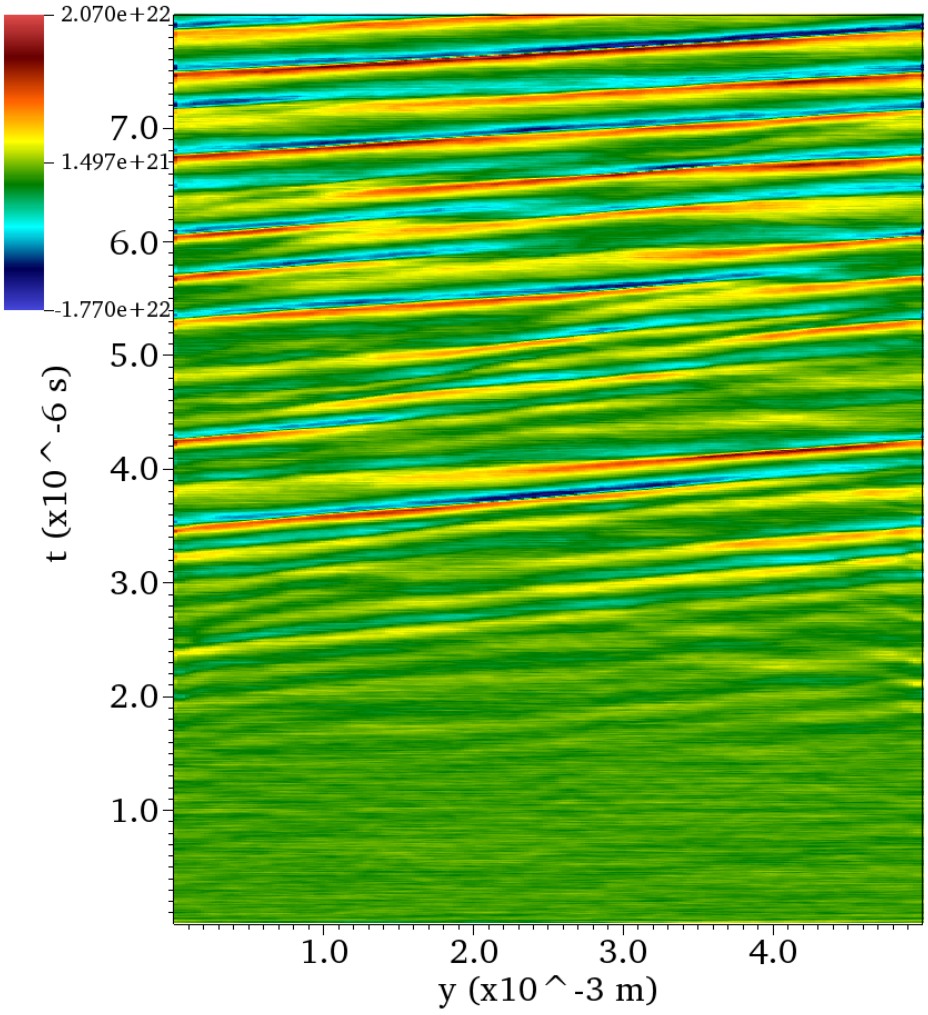

Figure 4.22: Contour plots of the spatial-temporal variation of the ion density multiplied by the azimuthal electric field $n_i(y,t)E_y(y,t)$ for the moment electron simulations.

CHAPTER 5

Conclusions and Future Directions

We have presented a numerical study of current driven instabilities and anomalous electron transport in the context of Hall-effect thrusters making use of the Thermophysics Universal Research Framework developed by the Air Force Research Lab. With the exception of a few modifications, the simulations are similar to the work presented by [Lafleur et al., 2016a] in the collisionless limit and have shown a direct correlation between a cross-field electron transport and the presence of azimuthal electrostatic instabilities. The instability properties are in good agreement with the analytical and numerical results of the past, and the anomalous electron mobility provides reasonable agreement with experimental measurements conducted. In addition to confirming the results of [Lafleur et al., 2016a], a number of numerical experiments are conducted in order to assess different possibilities for a reduced order electron mobility model. Below we outline the major shortcomings of the simulations and provide a short discussion on the future direction of this investigation.

In the short term, the implementation of electron-neutral collisions is an obvious direction for improvement of our simulations. The addition of a standard Monte Carlo Collision algorithm for electrons presented by [Okhrimovskyy et al., 2002] will allow us to investigate the behavior of the instability when damped by classical collisions as well as the electron mobility predicted classically due to momentum transfer collisions. Used in conjunction with ionization and excitation collision rates, a more robust investigation of Landau damping oscillations can be conducted and compared to experimental measurements of a spoke mode.

Simulations where Poisson's equation is solved only in the azimuthal direction assume the radial and axial wave numbers are negligible. Doing so, ignores any fluctuations in electric field which may occur in either of the two remaining directions. Though improvements to

the initial condition and the particle boundary conditions have been made, the convection of the instability cannot be accurately simulated without the solving of Poisson's equation in both the azimuthal $\hat{y}$ and axial $\hat{z}$ directions. Because the framework implemented already requires a three dimensional tracking of positions and velocities, the modification to Poisson's equation, is in theory, simple within our framework. The issue remains that to simulate the ion acoustic wave in two dimensions for multiple Landau oscillation frequencies is computationally expensive. As mentioned in the introductory remarks, many authors including [Ahedo et al., 2003] and [Raitses et al., 2005] have argued the importance of wall sheath physics in the Hall-effect thruster channel playing a significant role in the anomalous mobility. If the electron interaction with the channel walls are not negligible, three dimensional, full kinetic simulation would likely be required to conduct predictive, non empirical simulations of a Hall-effect thruster. Despite the work still required, the simple azimuthal current driven instability simulations presented here has provided insight into the importance of wave induced transport and significant progress has been made towards the development of a predictive electron transport model.

References

[Adam et al., 2004] Adam, J. C., Héron, A., and Laval, G. (2004). Study of stationary plasma thrusters using two-dimensional fully kinetic simulations. *Physics of Plasmas*, 11(1):295–305.

[Ahedo et al., 2003] Ahedo, E., Gallardo, J. M., and Martinez-Sanchez, M. (2003). Effects of the Radial Plasma-Wall Interaction on the Hall Thruster Discharge. *Physics of Plasmas*, 10(8).

[Ahedo and Martinez-Sanchez, 1998] Ahedo, E. and Martinez-Sanchez, M. (1998). One-dimensional Plasma Structure in Hall Thrusters. *AIAA/ASME/SAE/ASEE Joint Propulsion Conference and Exhibit, 34th, Cleveland, OH, July 13-15, 1998*, (1):AIAA–1998–8788.

[Araki et al., 2016] Araki, S. J., Martin, R. S., Bilyeu, D., and Koo, J. W. (2016). SM/MURF: Current Capabilities and Verification as a Replacement of AFRL Plume Simulation Tool COLISEUM. *52nd AIAA/SAE/ASEE Joint Propulsion Conference*.

[Barral et al., 2003] Barral, S., Makowski, K., Peradzyński, Z., Gascon, N., and Dudeck, M. (2003). Wall Material Effects in Stationary Plasma Thrusters. II. Near-wall and In-wall Conductivity. *Physics of Plasmas*, 10(10):4137–4152.

[Birdsall and Langdon, 1991] Birdsall, C. K. and Langdon, A. B. (1991). *Plasma Physics via Computer Simulation*. Taylor and Francis Group, New York.

[Boeuf, 2014] Boeuf, J.-p. (2014). Rotating Structures in Low Temperature Magnetized Plasmas-insight from Particle Simulations. *Frontiers in Physics*, 2(December):1–17.

[Boeuf and Garrigues, 1998] Boeuf, J. P. and Garrigues, L. (1998). Low Frequency Oscillations in a Stationary Plasma Thruster. *Journal of Applied Physics*, 84(7):3541.

[Brieda, 2005] Brieda, L. (2005). *Development of the DRACO ES-PIC Code and Fully-Kinetic Simulation of Ion Beam Neutralization*. M.s., Virginia Tech.

[Buneman, 1963] Buneman, O. (1963). Excitation of Field Aligned Sound Waves by Electron Streams. *Physical Review Letters*, 10.

[Choueiri, 2004] Choueiri, E. Y. (2004). A Critical History of Electric Propulsion: The First 50 Years. *Journal of Propulsion and Power*, 20.

[Cunningham et al., 2016] Cunningham, D. A., Liu, D., Hartsfield, C., Mullins, C., Farnell, C., Williams, J. D., and Hargus, W. A. (2016). Synchronized Measurement of Plasma Characteristics In a Hall Effect Thruster. *54th AIAA Aerospace Sciences Meeting*.

[Davidson, 1972] Davidson, R. (1972). *Methods in Nonlinear Plasma Theory*. Academic Press, New York.

[Dum, 1970] Dum, C. T. (1970). Nonlinear Stabilization of High-Frequency Instabilities in a Magnetic Field. *Physics of Fluids*, 13(8):2064.

[Fife et al., 1997] Fife, J. J., Martinez-Sanchez, M., Szabo, J., Fife, J. J., Martinez-Sanchez, M., and Szabo, J. (1997). A Numerical Study of Low-frequency Discharge Oscillations in Hall Thrusters. In *33rd Joint Propulsion Conference and Exhibit*, pages AIAA–1997–3052.

[Fife and Martinez-Sanchez, 1998] Fife, J. M. and Martinez-Sanchez, M. (1998). Hybric-PIC Modeling and Electrostatic Probe Survey of Hall Thrusters.

[Fried and Conte, 1961] Fried, B. D. and Conte, S. D. (1961). *The Plasma Dispersion Function*. New York.

[Gildea et al., 2009] Gildea, S. R., Batishchev, O., and Martinez-Sanchez, M. (2009). Fully Kinetic Modeling of Divergent Cusped Field Thrusters .

[Goebel and Katz, 2008] Goebel, D. M. and Katz, I. (2008). *Fundamentals of Electric Propulsion: Ion and Hall Thrusters*.

[Koo and Boyd, 2006] Koo, J. W. and Boyd, I. D. (2006). Modeling of Anomalous Electron Mobility in Hall Thrusters. *Physics of Plasmas*, 13(3).

[Krall et al., 1974] Krall, N. A., Trivelpiece, A. W., and Symon, K. R. (1974). Principles of Plasma Physics.

[Lafleur et al., 2016a] Lafleur, T., Baalrud, S. D., and Chabert, P. (2016a). Theory for the Anomalous Electron Transport in Hall Effect thrusters. I. Insights from particle-in-cell Simulations. *Physics of Plasmas*, 23(5).

[Lafleur et al., 2016b] Lafleur, T., Baalrud, S. D., and Chabert, P. (2016b). Theory for the Anomalous Electron Transport in Hall Effect Thrusters. II. Kinetic Model. *Physics of Plasmas*, 23(5).

[Lampe et al., 1971] Lampe, M., Manheimer, W. M., McBride, J. B., Orens, J. H., Shanny, R., and Sudan, R. N. (1971). Nonlinear Development of the Beam-Cyclotron Instability. *Physical Review Letters*, 26(20):1221–1225.

[McDonald and Gallimore, 2011] McDonald, M. S. and Gallimore, A. D. (2011). Parametric Investigation of the Rotating Spoke Instability in Hall Thrusters. *32nd International Electric Propulsion Conference*.

[Mikellides and Katz, 2012] Mikellides, I. G. and Katz, I. (2012). Numerical Simulations of Hall-effect Plasma Accelerators on a Magnetic-field-aligned Mesh. *Physical Review E*, 86.

[Okhrimovskyy et al., 2002] Okhrimovskyy, A., Bogaerts, A., and Gijbels, R. (2002). Electron Anisotropic Scattering in Gases: A Formula for Monte Carlo Simulations. *Physical Review E*.

[Raitses et al., 2005] Raitses, Y., Staack, D., Keidar, M., and Fisch, N. J. (2005). Electron-Wall Interaction in Hall Thrusters. *Physics of Plasmas*, 12(057104).

[Sagdeev, 1966] Sagdeev, R. (1966). Cooperative Phenomena and Shock Waves in Collisionless Plasmas. *Reviews of Plasma Physics*, 4.

[Sekerak et al., 2013] Sekerak, M. J., Longmier, B. W., Gallimore, A. D., Brown, D. L., Hofer, R. R., and James E. Polk (2013). Azimuthal Spoke Propagation in Hall Effect Thrusters. *33rd International Electric Propulsion Conference*.

[Stringer, 1964] Stringer, T. (1964). Electrostatic Instabilities in Current-Carrying and Counterstreaming Plasmas. *Journal of Nuclear Energy. Part C*, 6.

[Tsikata et al., 2014] Tsikata, S., Cavalier, J., Héron, A., Honoré, C., Lemoine, N., Grésillon, D., and Coulette, D. (2014). An Axially Propagating Two-stream Instability in the Hall Thruster Plasma. *Physics of Plasmas*, 21.